

Chapter 4

Mechanistic Investigations of Ni-Catalyzed Asymmetric Reductive Cross-Couplings with Alkenyl Bromide Electrophiles[‡]

4.1 INTRODUCTION

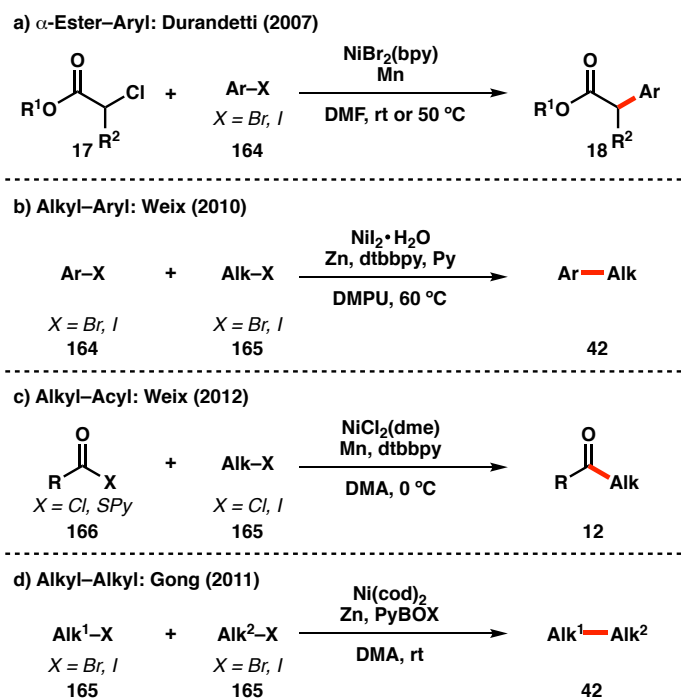
4.1.1 Recent Advances in Reductive Cross-Couplings

Nickel-catalyzed reductive cross-couplings have recently gained prominence as mild methods for the construction of C–C bonds. These cross-electrophile couplings use a stoichiometric reductant (typically Zn or Mn) to turn over the Ni catalyst, and commonly employ two electrophiles that are distinguished by their hybridization to afford good levels of cross-selectivity.¹ The Durandetti, Weix, and Gong groups have reported cross-couplings between a variety of different electrophile classes, including α -ester-aryl,²

[‡]The research presented in this chapter was completed in collaboration with: 1) Alan H. Cherney (graduate student) and Raymond Turro (graduate student) in the Reisman group, as well as Yunfang Yang (postdoctoral scholar) and Xin Hong (graduate student) in the Houk group.

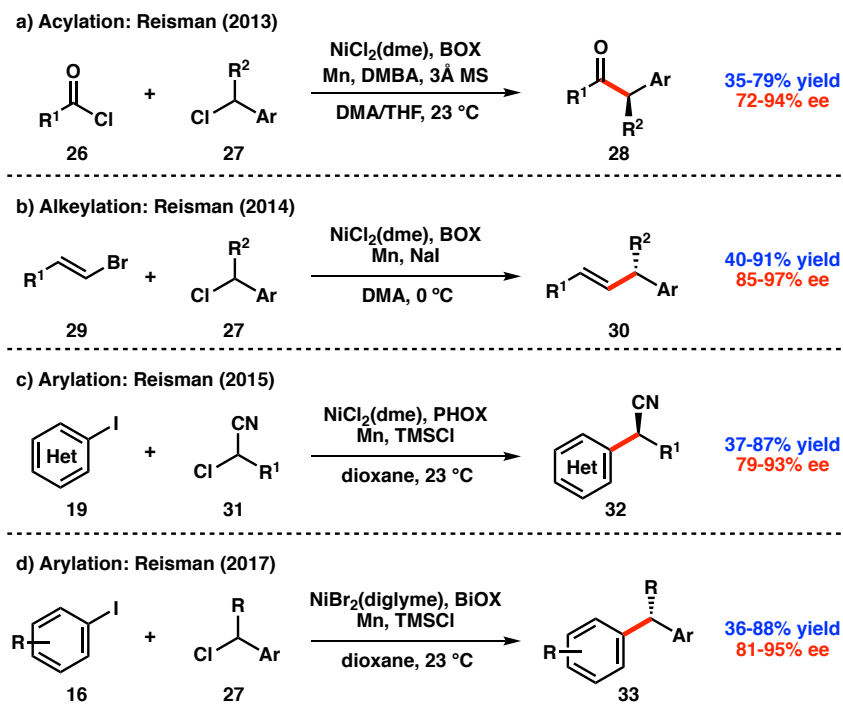
alkyl–aryl,^{3,4} alkyl–acyl,⁵ and alkyl–alkyl⁶ cross-couplings (Scheme 4.1). The mild reaction conditions allow for excellent functional group tolerance and eliminate the need to form air sensitive and highly reactive organometallic reagents typically employed in conventional cross-coupling reactions.

Scheme 4.1 Select examples of reductive cross-couplings of organic electrophiles.



The ability to utilize C(sp³)-hybridized electrophiles in reductive cross-couplings has also allowed for the design of asymmetric approaches. Our laboratory has recently developed a variety of asymmetric cross-couplings between C(sp²)-hybridized (acyl chlorides,⁷ alkenyl bromides,^{8–10} and (hetero)aryl iodides^{11,12}) and C(sp³)-hybridized (benzyl chlorides, α -chloronitriles) electrophiles (Scheme 4.2). These reactions typically proceed in good yield and provide the desired products with good to excellent enantioselectivities when chiral BOX, BiOX, or PHOX ligands are used.

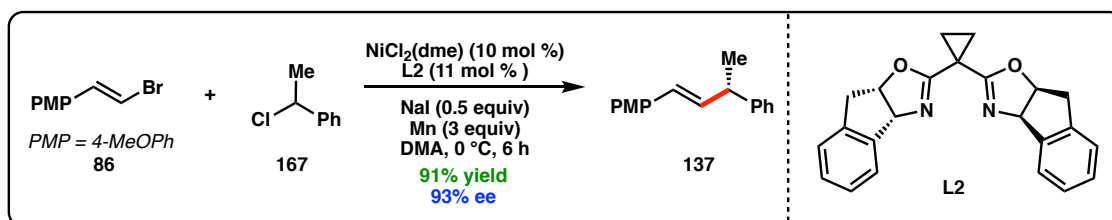
Scheme 4.2 Asymmetric reductive cross-couplings of organic electrophiles.



While a wide variety of electrophiles and methods have been reported, there are only a few in-depth mechanistic studies regarding these types of transformations, most of which focus on achiral reactivity.^{4,13,14} In order to better understand the origins of cross-selectivity and enantioselectivity in asymmetric reductive cross-couplings, we set out to conduct a mechanistic study on the asymmetric Ni-catalyzed alkenylation reaction between alkenyl bromide **86** and benzyl chloride **167** which was previously disclosed from our laboratory in 2014 (Scheme 4.3).⁸ The Ni-catalyzed cross-coupling reaction proceeds in good yields and with excellent enantioselectivities when chiral BOX ligand **L2** is used in conjunction with NiCl₂(dme) as a precatalyst. During the optimization of this reaction, DMA was found to be the most optimal solvent. The use of Mn affords turnover of the Ni catalyst, while the addition of NaI and low reaction temperature afford higher yields of the

desired cross-coupled product. In order to obtain a more holistic mechanistic study, we not only conducted experimental work in our laboratory, but also collaborated with Prof. Kendall Houk at UCLA in order to conduct computational studies. Herein, we describe the results of these studies and provide additional insight into the likelihood of potential reaction mechanisms.

Scheme 4.3 Ni-catalyzed alkenylation reaction as the subject of our studies.

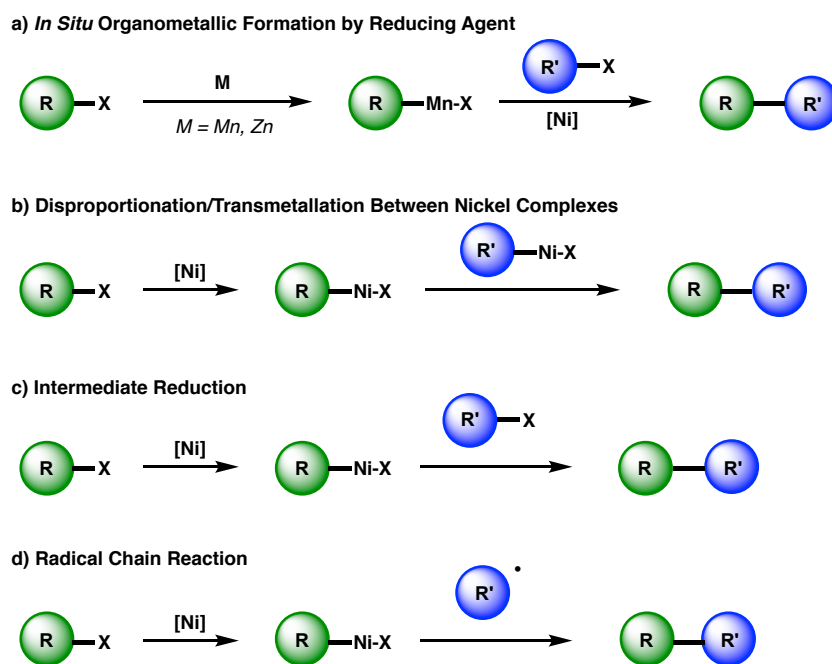


4.2 PROPOSED REACTION MECHANISMS

Weix and co-workers were the first to conduct an in-depth mechanistic study on the Ni-catalyzed reductive cross-coupling between C(sp²)-hybridized and C(sp³)-hybridized electrophiles.^{1,4,13} They initially proposed four possible reaction mechanisms for the reductive cross-coupling of aryl iodides and alkyl iodides (Scheme 4.1b): 1) *in situ* organometallic formation, 2) disproportionation/transmetalation, 3) intermediate reduction, and 4) radical chain (Figure 4.1).⁴ A series of experimental mechanistic studies revealed the reductive cross-coupling between aryl halides and alkyl halides was most consistent with a radical chain mechanism.¹³ Gong and co-workers, however, further studied the intermediate reduction and radical chain mechanisms via computational studies, and found both to be thermodynamically feasible when the C(sp²)-hybridized

electrophile was the first to undergo oxidative addition.¹⁴ These studies were conducted on the reductive aryl–alkyl coupling, however it is possible that the reaction mechanism varies for the other nickel-catalyzed reductive cross-coupling reactions, given the differences in electrophile identity, reported ligands, and reaction conditions. The four mechanistic proposals outlined by Weix and coworkers will be discussed in greater detail in the following sections, however in order to maintain clarity throughout the duration of this chapter, analogous ligands and electrophiles consistent with the alkenylation reaction in Scheme 4.3 will be used.

Figure 4.1 Proposed mechanisms for Ni-catalyzed reductive cross-coupling.

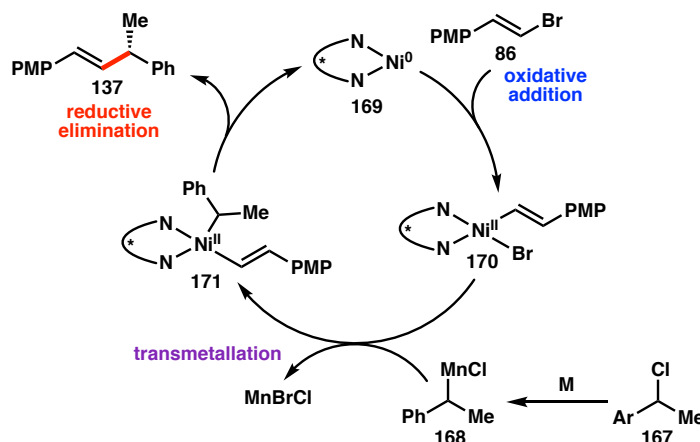


4.2.1 *In Situ* Organometallic Formation

One possible reaction mechanism is the *in situ* formation of organometallic species **168** from Zn or Mn insertion into the benzyl halide bond (Figure 4.2). The remaining steps in this mechanism involve oxidative addition (**169** to **170**), transmetalation (**170** to **171**),

and reductive elimination (**171** to **169**), similar to conventional redox neutral cross-coupling. While Zn or Mn can be used as heterogeneous reductants to shuttle electrons to the Ni catalyst, a variety of reductive cross-couplings have been shown to proceed with soluble organic reductants (i.e. tetrakis(dimethylamino)ethylene, TDAE).^{8,10,15} Although a number of published methods depict examples describing the feasibility of forming benzylic organomanganese species,^{16–19} Weix and co-workers demonstrated that the formation of organozinc was low under their reaction conditions.¹³ Taken together, while this mechanism may be operable, if not in some level, in Ni-catalyzed reductive-cross couplings, it is typically disregarded when potential mechanisms are proposed for this class of reactions.

Figure 4.2 In-situ organometallic formation mechanism.

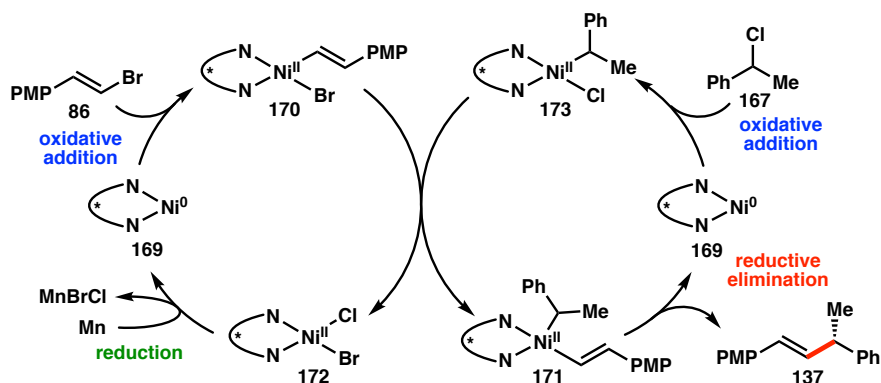


4.2.2 Disproportionation/Transmetalation

A second possible mechanism is the transmetalation and ligand exchange between two distinct Ni(II) oxidative addition complexes (Figure 4.3). Each electrophile (**86** and **167**) undergoes oxidative addition to Ni(0) complex **169** to afford **170** and **173**, which then

disproportionate to afford Ni(II) complex **171** containing both the aryl and alkenyl groups. The desired product **137** is formed by reductive elimination from complex **171**. If ligand exchange is the rate-determining step in the reaction (which is likely, given that this step is bimolecular between two catalytically generated species), one would expect to see a kinetic second order dependence on nickel.²⁰ In the case of an asymmetric reductive cross-coupling, a non-linear effect in the product enantioselectivity would also be observed if ligand exchange (from **170** and **173** to **172** and **171**) were the enantiodetermining step. Finally, this disproportion/transmetalation mechanism forms **137** via reductive elimination from a Ni(II) species, which is significantly harder to achieve compared to reductive elimination from a Ni(III) species.

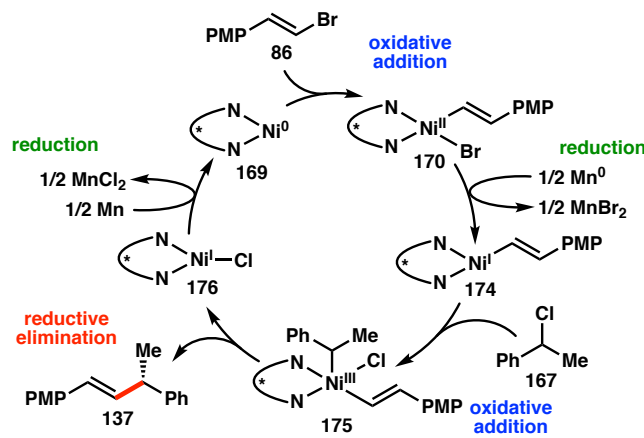
Figure 4.3 Disproportionation/transmetalation mechanism.



4.2.3 Intermediate Reduction

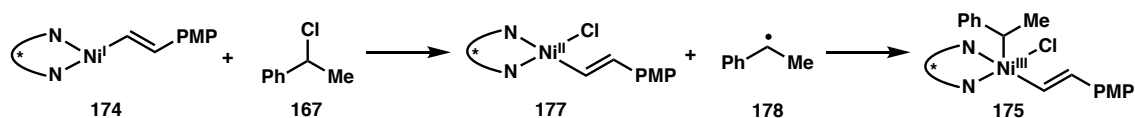
A third possible mechanism is the intermediate reduction mechanism (Figure 4.4). Aryl halide **86** undergoes a concerted oxidative addition to Ni(0) complex **169**, followed by an intermediate reduction step. The resultant Ni(I) species **174** can undergo a second, single-electron oxidative addition with alkyl halide **167** to afford Ni(III) complex

Figure 4.4 Sequential oxidative addition mechanism.



175, which can produce cross-coupled product **86** following reductive elimination. A two-step oxidative addition of the alkyl chloride, first by halide abstraction followed by recombination of alkyl radical **178** to Ni(II) center **177**, allows for stereoconvergence in the mechanism (Figure 4.5).

Figure 4.5 Two-step radical-type oxidative addition of the alkyl halide.

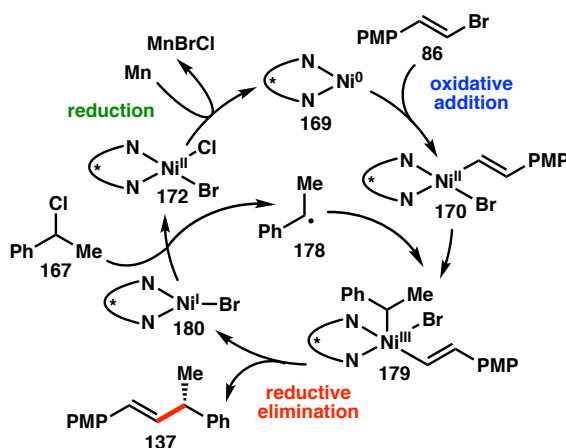


4.2.4 Radical Chain

The fourth possible mechanism for consideration, through a radical chain type processes (Figure 4.6), is distinctive from the sequential oxidative addition mechanism by the lifetime of alkyl radical **178**. Instead of the alkyl radical adding to the same Ni(II) center (**172**) that abstracted the halide atom, the alkyl radical can undergo cage escape and intercept a different Ni(II) center (**170**) to afford Ni(III) complex **175** that can provide cross-coupled product **86** following reductive elimination. This mechanism is often

distinguished from sequential oxidative addition by the use of a radical clock probe. The rearrangement of a radical clock substrate under the reaction conditions is simply used to identify the presence of a radical species. However, a difference in the ratio of rearranged to unarranged products at varying concentrations of Ni provides evidence for radical chain mechanism when rearranged products dominate at lower Ni loadings.

Figure 4.6 Radical chain mechanism.



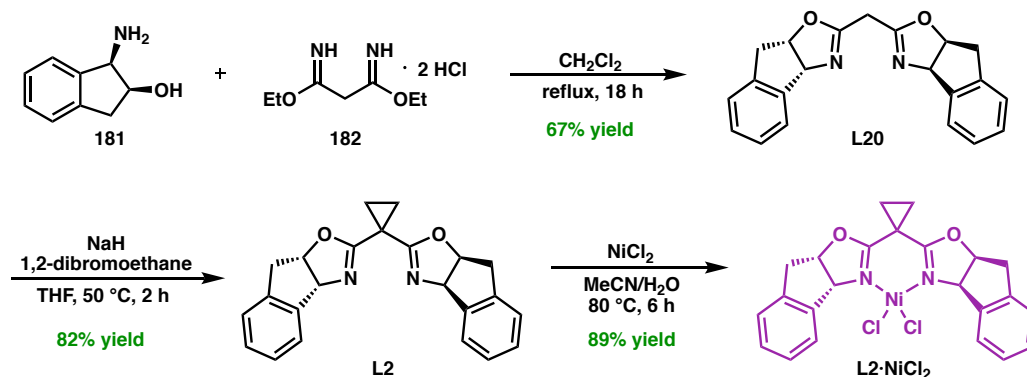
4.3 EXPERIMENTAL STUDIES: NICKEL COMPLEXES

4.3.1 Synthesis and Characterization of Ni(II) Complexes

We began our investigations by preparing **L2**·NiCl₂ (Scheme 4.4). Condensation of (*1R,2S*)-(+)-cis-1-amino-2-indanol (**181**) with diethyl malonimidate dihydrochloride (**182**) provided BOX ligand **L22** in 67% yield. Deprotonation of the methylene linker with sodium hydride and substitution with 1,2-dibromoethane afforded desired BOX ligand **L2** in 82% yield. Finally, metalation with NiCl₂ in acetonitrile and water at elevated temperatures provided the purple **L2**·NiCl₂ complex in 89% yield, and following

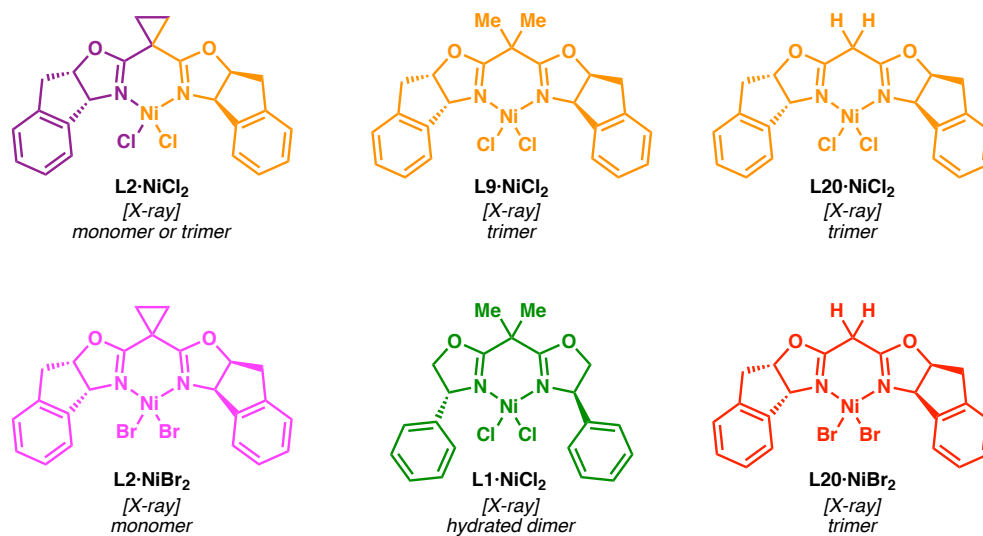
recrystallization we were able to confirm its structure via X-ray crystallography. The monomeric $\mathbf{L2} \cdot \text{NiCl}_2$ complex crystallized in the orthorhombic $P2_12_12_1$ space group as a distorted tetrahedral complex. Analysis by ^1H NMR reveals broad proton signals, including two resonances at 56 and -109 ppm which confirm the structure as a high-spin paramagnetic complex.

Scheme 4.4 Synthesis of $\mathbf{L2} \cdot \text{NiCl}_2$ complex.



Recrystallization of $\mathbf{L2} \cdot \text{NiCl}_2$ occasionally provided orange crystals instead of purple crystals. Analysis by X-ray crystallography revealed that $\mathbf{L2} \cdot \text{NiCl}_2$ could also crystallize as a trimeric complex containing two pentavalent Ni centers and one hexavalent Ni center bridged by the chloride ligands. A series of other Ni dihalide complexes were also prepared and analyzed by X-ray crystallography (Figure 4.7). Depending on the identity of the linker, halide, and chiral pocket (indanyl vs. phenyl), a variety of Ni geometries could be obtained upon crystallization (monomer, hydrated dimer, or trimer). Typically purple or pink crystals were monomeric complexes, green crystals were hydrated dimeric complexes, and either orange or red crystals were trimeric complexes. When trimeric $\mathbf{L2} \cdot \text{NiCl}_2$ was dissolved and recrystallized, the monomeric species was often afforded, indicating the aggregation state is an artifact of the crystallization conditions.

Figure 4.7 Prepared Ni dihalide complexes and their corresponding geometries.

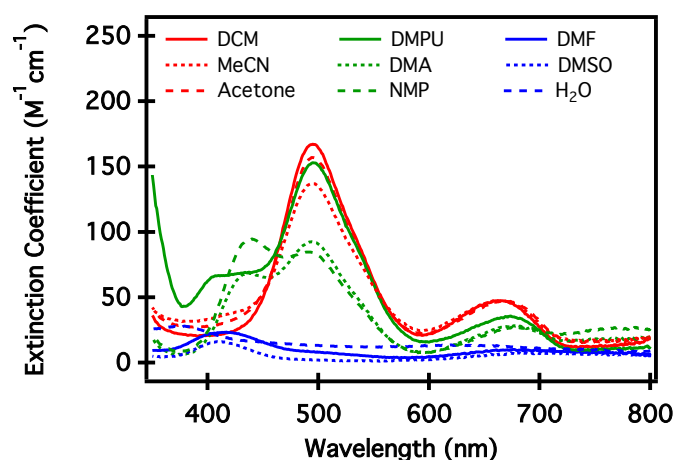


4.3.2 UV-Vis Spectroscopy

With **L2**·NiCl₂ in hand, we turned our attention to studying its properties. Dissolving complex **L2**·NiCl₂ in a variety of solvents at a concentration of 1 mg/mL revealed a chromatic solvent effect, which ranged from pink to orange to colorless solutions. Both the monomeric and trimeric **L2**·NiCl₂ complexes provided the same results, demonstrating they converge to the same species while in solution. Electronic absorption spectra were collected in a variety of solvents as shown in Figure 4.8. The extinction coefficient ($M^{-1}cm^{-1}$) reaches a maximum at 500 nm and 670 nm when **L2**·NiCl₂ is dissolved in DCM, MeCN, and acetone. Switching to more polar solvents such as DMPU (a urea), DMA, and NMP (both amides), absorption decreases in the 500 nm and 670 nm bands and a new absorption band forms at 360 nm, indicating the observation is not due to solvatochromism.²¹ This may potentially be an indication of solvent binding to the Ni center. Other solvents such as DMF, DMSO, and H₂O lose nearly all absorption in the

visible spectrum as evidenced by colorless solutions. While the origin of this solvent effect is not yet understood, it may provide insight into the solvent effects realized upon initial reaction optimization (DMA provided the highest product yield, while NMP and DMPU provided the second highest yields).⁸

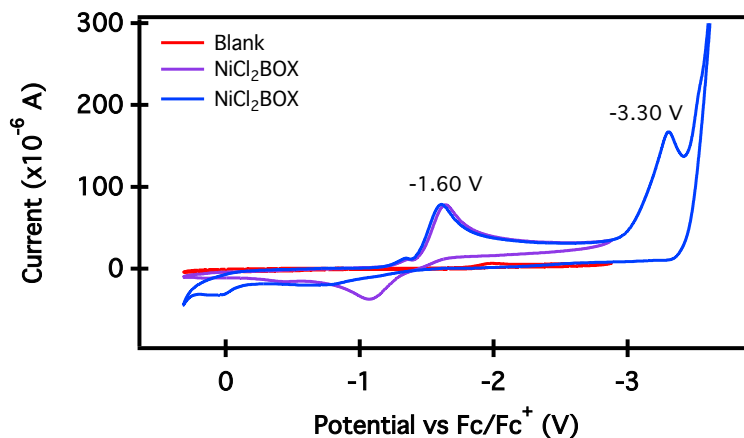
Figure 4.8 Electronic absorption spectra of $L2 \cdot NiCl_2$.



4.3.3 Cyclic Voltammetry

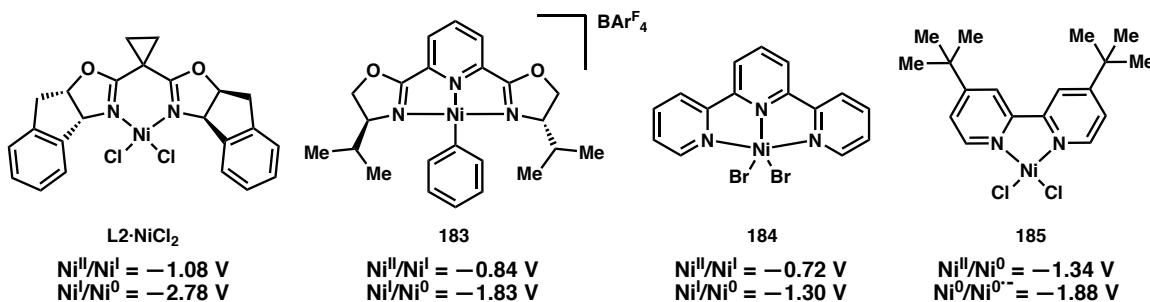
We then set out to analyze $L2 \cdot NiCl_2$ by cyclic voltammetry (CV) (Figure 4.9). When $L2 \cdot NiCl_2$ was analyzed at a concentration of 1.0 mM in DMA with 0.1 M Bu_4NPF_6 as the supporting electrolyte, we observed a quasi-reversible redox couple with the cathodic peak reaching a maximum at -1.60 V, as well as an irreversible redox process with a maximum cathodic peak at -3.30 V vs. the ferrocene/ferrocenium redox couple (Fc/Fc^+). This concentration corresponds to a 0.1 mol % loading of Ni under the published reaction conditions. Amperometry measurements for the first reduction peak are most consistent with a one-electron reduction process, therefore we have assigned these two reduction peaks as the Ni^{II}/Ni^I and Ni^I/Ni^0 redox couples, respectively. The cathodic peak at -1.60 V

Figure 4.9 Cyclic voltammetry of $L2 \cdot NiCl_2$.



happens to also be the same reduction potential for the two-electron oxidation of Mn.²² In contrast to bipyridine ligands which show redox activity in the absence of bound metal species, cyclic voltammetry of the free bis(oxazoline) ligand **L2** shows no redox activity, indicating **L2** may be innocent in the reduction process. The one-electron reduction potentials were converted relative to standard calomel electrode (SCE) and compared to known reduction potentials of other Ni(II) complexes containing pyridine-containing ligands (Figure 4.10).^{23–26} The $L2 \cdot NiCl_2$ complex displays a significantly stronger Ni^I/Ni^0 redox couple compared to **L2** and **L2**, however bipyridine complex **L2** displays a weaker

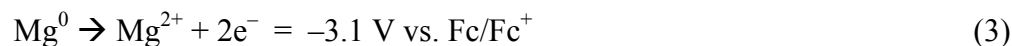
Figure 4.10 Reported reduction potentials of bidentate and tridentate N-bound Ni complexes used in cross-coupling reactions.



reduction potential to access Ni(0), however it proceeds via a two-electron reduction from Ni(II) to Ni(0). No reduction potentials of other bis(oxazoline) or bi(oxazoline) Ni dihalide complexes have been reported in literature.

4.3.4 EPR Spectroscopy

Further studies by electron paramagnetic resonance (EPR) spectroscopy probed the oxidation state of nickel following the reduction process at -1.6 V. A 10 mM solution of **L2** in DMA was reduced with 10 equivalents of Zn, Mn, or Mg under inert atmosphere for >12 hours to afford a dark orange solution. The reduction potentials for these three metals are shown in Equations 1–3.²² Subsequent filtering and analysis by EPR affords a Ni(I) spectrum (Figure 4.11) when Zn and Mg are used as the reductants, which we have

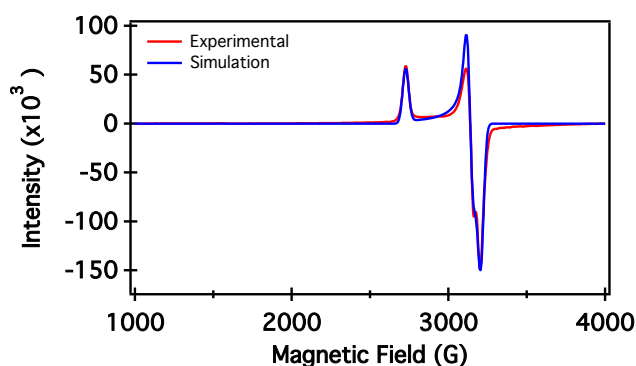


assigned as a **L2**·NiCl complex, however with an unknown geometry (monomeric or dimeric bridged species). When Mn is used as the reductant, the Ni(I) signal is obscured by MnCl₂, which is consequently EPR active. Attempts to remove background absorption by MnCl₂ reveals the presence of the same **L2**·NiCl complex.

The obtained Ni(I) spectrum has rhombic anisotropy, and simulations afford g values of 2.4879, 2.1588, and 2.1092 that correspond to a metal-centered radical.²⁷ This is in contrast to PyBOX and Tpy coordinated Ni(I) complexes that display a ligand-centered radical containing contributions from ¹⁴N hyperfine coupling.^{23,24} Interestingly, the same

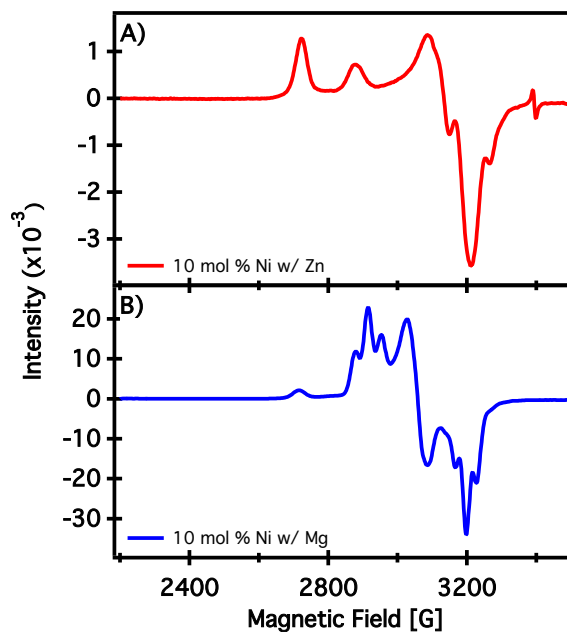
reduction reaction plates out Ni mirror with no observable Ni(I) signal when conducted with Zn as the reductant in either THF or a mixture of DCM and toluene.

Figure 4.11 EPR spectra for reduction of $\mathbf{L2}\cdot\text{NiCl}_2$ at 10 mM.



We then reduced $\mathbf{L2}\cdot\text{NiCl}_2$ for 9 hours at a concentration of 100 mM in DMA, which represents the concentration of Ni species in solution relevant to the catalytic system (10 mol % loading). When either Mg or Zn were used as the reductant, Ni(I) species were formed; however, the resulting EPR spectra were different than when conducted at 10 mM (Figure 4.12). With Zn, two Ni(I) species are formed in $\sim 2:1$ ratio with the major species being the previously observed Ni(I) complex. When Mg was used as the reductant, the previous Ni(I) complex was present, however only in trace quantities. A third Ni(I) complex becomes the major species in this reduction. Notably, there is more Ni(I) present in solution when Mg, the stronger reductant, is used; however, quantification of the signal in Figure 4.12b provides an approximate measurement which determines the signal accounts for only 10% of the available Ni species; the remaining 90% is either Ni(II), Ni(0), or a ferromagnetically coupled Ni(I) dimer. Nevertheless, these results demonstrate the possibility Ni(I) speciation at varying concentrations, and may indicate dimerization or aggregation of the catalyst. Further studies to elucidate these structures are necessary.

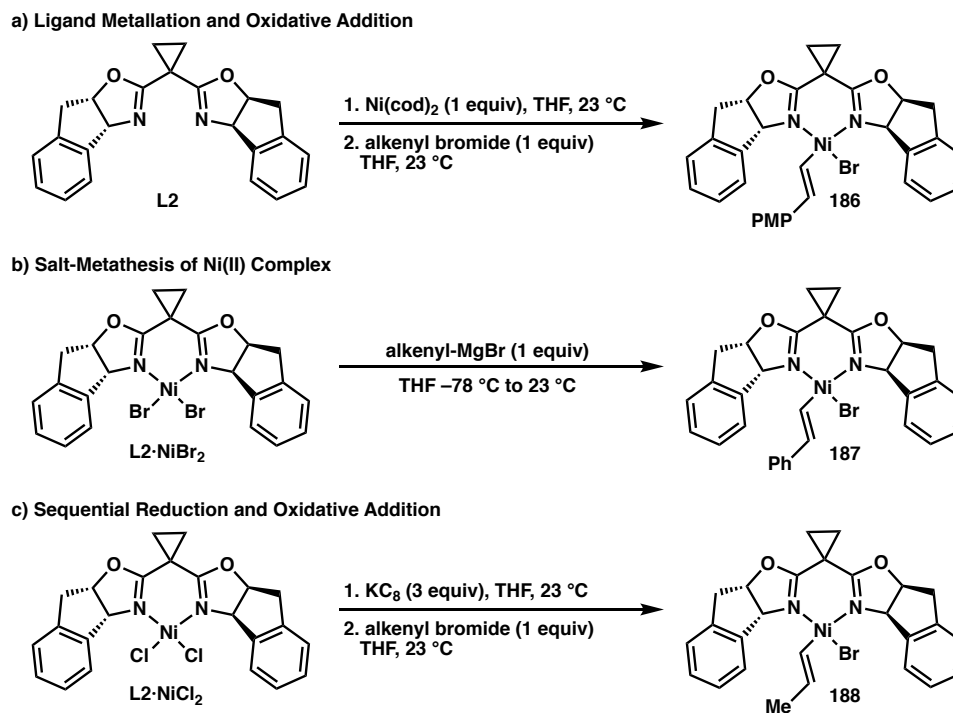
Figure 4.12 EPR spectra for reduction of $\mathbf{L2}\cdot\text{NiCl}_2$ at 100 mM.



4.3.5 Oxidative Addition Complexes

In addition to synthesizing $\mathbf{L2}\cdot\text{NiX}_2$ complexes, we also attempted to synthesize and characterize oxidative addition complexes (Scheme 4.5). Three different approaches were taken to generate these intermediates. We first tried to metalate BOX ligand $\mathbf{L2}$ with $\text{Ni}(\text{cod})_2$, followed by the addition of a stoichiometric amount of alkenyl halide $\mathbf{L2}$ for oxidative addition. Unfortunately, a large amount of homocoupled diene product was observed in this reaction. Our second approach involved the addition of a styrenyl Grignard reagent to $\mathbf{L2}\cdot\text{NiCl}_2$ to form the product through salt metathesis. While the crude sample was partially fractionated and analyzed by ^1H NMR and EPR spectroscopy, the resulting fractions were not clean. However, the identification of paramagnetic species suggests that the desired oxidative addition complex and undesired dialkenyl complex were possibly formed under the reaction conditions. Attempts to crystallize the Ni complexes provided

Scheme 4.5 Attempts at forming oxidative addition complexes.



solids that unfortunately powder diffracted when analyzed by X-ray diffraction. Lastly, we attempted to reduce $\text{L2}\cdot\text{NiCl}_2$ with a reductant (KC_8 used in excess), then filtered the solution and added alkenyl halide via an inverse addition protocol (Ni(0) added to electrophile). In all these approaches, we observed promising reactivity, however we were unsuccessful in purifying and crystallizing the Ni(II) oxidative addition complexes for X-ray crystallography. These reactions are by no means exhaustive, and future work dedicated to conducting similar transformations while carefully controlling cryogenic reaction and isolation temperatures may be more profitable.

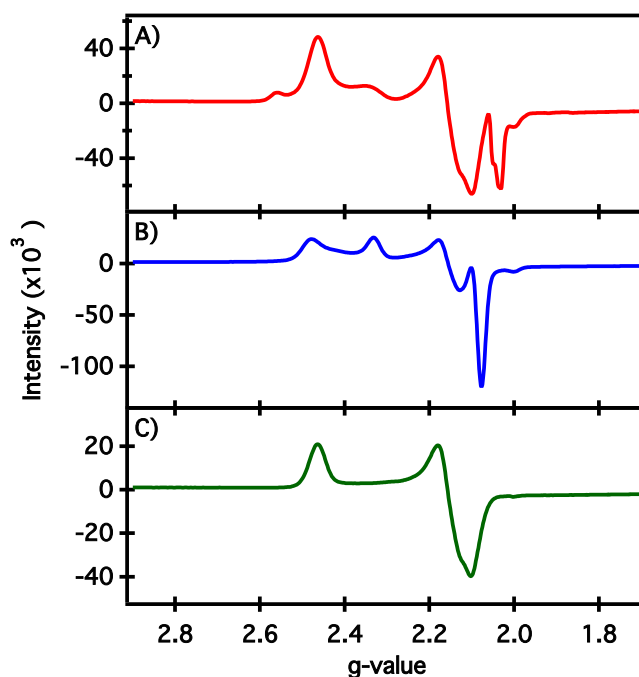
4.3.6 Analysis of Ni(I) Intermediates

Since we were unable to isolate Ni(II) oxidative addition complexes, we turned our attention to analyzing in-situ generated Ni(I) intermediates by EPR spectroscopy. By

mixing a solution of $\mathbf{L2}\cdot\text{Ni}(\text{cod})$, $\text{Ni}(\text{cod})_2$, and alkenyl bromide $\mathbf{L2}$ for 15 minutes in DMA under inert atmosphere, we were able to observe a mixture of Ni(I) signals by EPR spectroscopy (Figure 4.13a). Some of the resulting EPR signals corresponded to the $\mathbf{L2}\cdot\text{NiBr}$ intermediate prepared by Mg reduction of $\mathbf{L2}\cdot\text{NiBr}_2$ (Figure 4.13c), indicating the feasibility of oxidative addition of the alkenyl bromide to Ni(0) followed by subsequent reduction via a comproportionation type mechanism.

To further confirm the likelihood of comproportionation, an equimolar mixture of $\mathbf{L2}\cdot\text{Ni}(\text{cod})$ and $\mathbf{L2}\cdot\text{NiBr}$ was prepared and observed by EPR (Figure 4.13b). A mixture of two Ni(I) species are detected, one of which is the $\mathbf{L2}\cdot\text{NiBr}$ complex. The other Ni(I) species may be a cod ligated Ni(I) halide complex. In summary, Ni(0) is capable of reducing putative $\mathbf{L2}\cdot\text{NiBrR}_{\text{alkenyl}}$ intermediates, thus indicating the feasibility of this

Figure 4.13 EPR spectra demonstrating the feasibility of comproportionation.



reduction step in the mechanism. These studies suggest that the reduction of $\mathbf{L2}\cdot\text{NiBrR}_{\text{alkenyl}}$ and $\mathbf{L2}\cdot\text{NiBr}_2$ complexes occurs readily, while reduction of the $\mathbf{L2}\cdot\text{NiBr}$ occurs more slowly. However, under the catalytic conditions, in which there is an excess of Mn or Zn, it seems likely that $\mathbf{L2}\cdot\text{NiBrR}_{\text{alkenyl}}$ would be reduced by the heterogeneous reductant rather than $\mathbf{L2}\cdot\text{Ni}(0)$.

Finally, although we have observed Ni(I) signals by EPR, analysis of the catalytic cross-coupling reaction at 50% conversion with Zn as the reductant shows no EPR active intermediates, indicating that Ni(II) may be the resting state in the transformation. Therefore, if Ni(I) intermediates are formed in the reaction, they are not long-lived species.

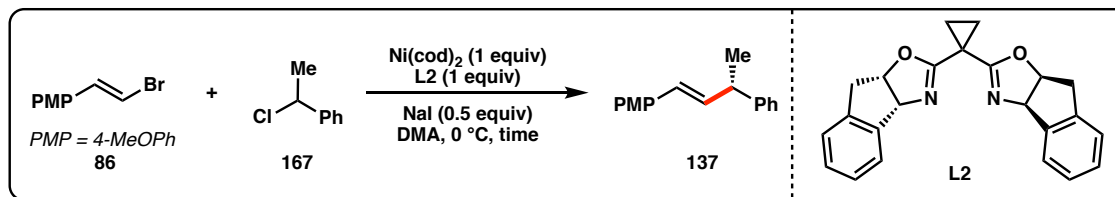
4.4 EXPERIMENTAL STUDIES: REACTION PROFILE

After conducting experimental studies on Ni intermediates, we turned our attention to studying the reaction process as a whole. These studies attempt to gain insight into factors that influence reaction yield and enantioselectivity.

4.4.1 Stoichiometric Ni(0) Studies

Since proposed mechanisms hypothesize that the $\text{C}(\text{sp}^2)$ -hybridized electrophile undergoes oxidative addition to a ligated Ni(0) complex, we decided to analyze the cross-coupling reaction in a system using stoichiometric Ni(0) in the form of $\text{Ni}(\text{cod})_2$ (Table 4.1). By using an equimolar mixture of alkenyl bromide **86**, benzyl chloride **167**, $\text{Ni}(\text{cod})_2$, and ligand **L2** in the absence of a heterogeneous metal reductant, we were able to produce the desired cross-coupled product in 48% yield and 97% ee after 6 hours (entry 1). Adding radical scavengers such as 9,10-dihydroanthracene (DHA) or butylated hydroxytoluene

Table 4.1. Alkenyl–benzyl cross-coupling with stoichiometric Ni(cod)₂.



Entry	Additive	Deviation from Conditions	Time (h)	Conv. (%) ^a	Yield (%)	ee (%)
1	—	—	6	98	48	97
2	DHA	—	6	52	49	96
3	BHT	—	6	91	54	96
4	CNB	—	6	48	0	—
5	—	no ligand	6	85	2	3
6 ^b	—	no NaI, premix 1 equiv Ni/L, then 86 and 167	6	47	28	83
7 ^{c,d}	—	no NaI, premix 2 equiv Ni/L, then 86, then 167	6	50	36	94
8 ^{c,d,e}	—	no NaI, premix 2 equiv Ni/L, then 167, then 86	6	88	5	91
9	—	—	24	100	78	96
10	DHA	—	24	100	79	96
11	BHT	—	24	100	77	96
12	galvinoxyl	—	24	60	57	96
13 ^f	TEMPO	—	24	86	42	96

^aBased off benzyl chloride. ^bNi and ligand prestired for 24 hours. ^cfirst electrophile stirred for 20 min. ^dNi and ligand prestired for 15 hours. ^e47% yield homocoupling of **167** observed. ^fbenzyl–TEMPO adduct detected by ¹H NMR.

(BHT) did not affect the reaction yield (entries 2 and 3), however adding an electron transfer inhibitor, 1-chloro-2,4-dinitrobenzene (CNB), completely shut down productive reactivity (entry 4). These results are similar to those obtained in the catalytic nickel coupling,⁸ and may be indicative of a similar reaction pathway. Interestingly, the reaction does not proceed in the absence of ligand, indicating that Ni(cod)₂ is not a sufficient “catalyst” to perform the cross-coupling (entry 5). During these reactions we visually observed slow dissolution of Ni(cod)₂ which may be critical for obtaining high ee of **137**. If Ni(cod)₂ and **L2** are premixed, the ee of **137** is slightly diminished (entry 6).

Since we were unsuccessful at isolating Ni(II) oxidative addition complexes, we set out to make the corresponding Ni(II) complexes in-situ. Forming the Ni(0) complex in-

situ, followed by the addition of each electrophile to the reaction sequentially, affords 36% yield of the desired cross-coupled product when the alkenyl bromide is added 20 minutes before the benzyl chloride (entry 7). Conversely, when the benzyl chloride is added to the reaction 20 minutes prior to the addition of the alkenyl bromide, only a 5% yield of product is observed and the majority of the benzyl chloride reacts to form the benzyl homocoupling product (entry 8). These observations are analogous to the stoichiometric Ni(II) oxidative addition study conducted by Weix and co-workers and suggest that the C(sp²) partner is the first electrophile to undergo oxidative addition.¹³

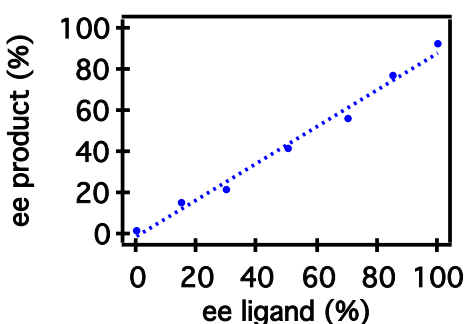
In order to improve the yield of **137**, we found that better conversion and higher yields could be obtained by running the reaction for 24 hours instead of 6 hours, affording 78% yield of the product in 96% ee. Again, the addition of radical inhibitors such as DHA or BHT did not shut down reactivity, however the addition of free radicals such as galvinoxyl and TEMPO decreased the yield of **137**, partially due to decreased conversion of the electrophiles. When TEMPO was added to the reaction, the TEMPO–benzyl adduct was detected by ¹H NMR spectroscopy, providing evidence for the formation of a discrete benzyl radical intermediate. Given these results, again we propose a comproportionation mechanism between the alkenyl bromide oxidative addition complex and exogenous Ni(0) to afford the Ni(I) alkenyl intermediate. Subsequent oxidative addition of the benzyl chloride, followed by reductive elimination, could afford the desired product.

4.4.2 Scalemic Ligand Study

Next we investigated how the product ee changed upon altering the ee of the ligand through the systematic preparation of scalemic mixtures of both ligand enantiomers (Figure

4.14). As the ee of **L2** increases from 0 to 100% ee, the ee of **137** also increases linearly. This not only shows that one ligand is bound to Ni during the enantiodetermining step of the reaction, but also likely eliminates the possibility that the reaction proceeds via the disproportionation/transmetalation mechanism.

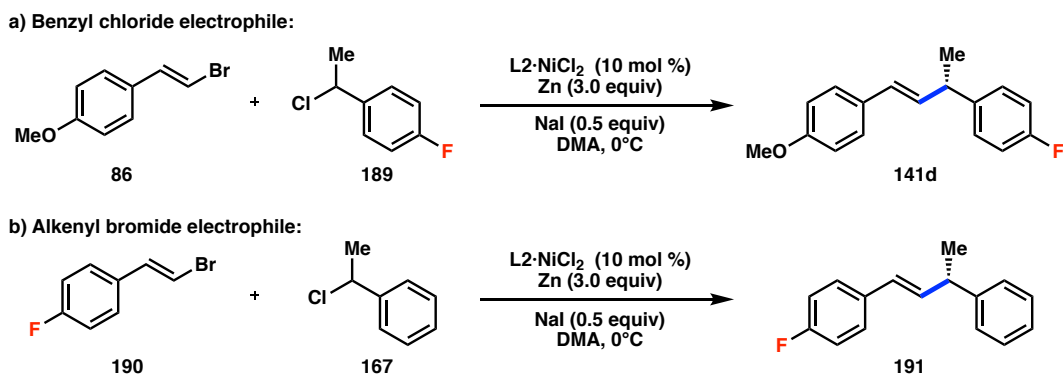
Figure 4.14 Scalemic ligand study.



4.4.3 Reaction Progress by ^{19}F NMR

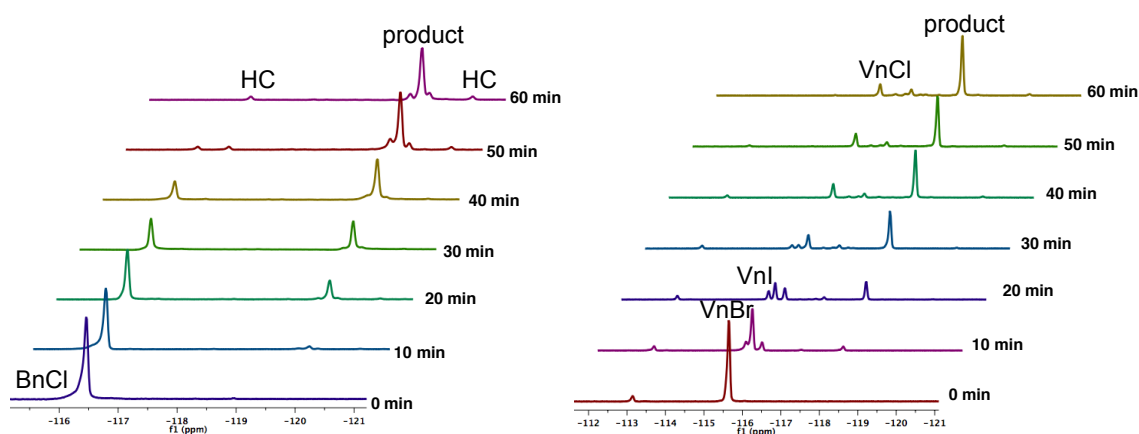
We briefly investigated the catalytic reaction with Zn as the reductant by analyzing aliquots by ^{19}F NMR. A fluorine atom was added to either the benzylic chloride electrophile (**189**) or the alkenyl bromide electrophile (**190**) to easily visualize the product distribution (Scheme 4.6). When **141d** was analyzed, rapid decrease of the starting material

Scheme 4.6 Cross-coupling reactions with fluorinated electrophiles.



was met with concomitant formation of the desired product. Side products that could be visualized included both diastereomers of the benzylic homocoupling product (Figure 4.15). In contrast, when **191** was analyzed, the alkenyl bromide converted to the desired product and also formed halide exchange products resulting in the corresponding alkenyl chloride and alkenyl iodide. While alkenyl iodide was consumed, alkenyl chloride persisted, indicating it is not catalytically reactive under the reaction conditions.

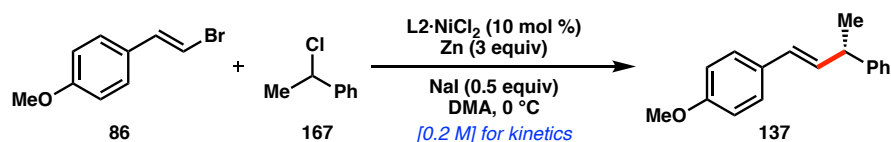
Figure 4.15 Benzyl chloride (left) and alkenyl bromide (right) probes by ^{19}F NMR.



4.4.4 Reaction Kinetics

We then turned our attention towards reaction kinetics to determine how the equivalents of each reagent effected the observed rate of product formation (Scheme 4.7). By conducting the cross-coupling reaction on a larger scale at a more dilute concentration (0.2 M compared to 1 M in the original report),⁸ we could effectively analyze aliquots of

Scheme 4.7 Standard reaction conditions for kinetic analysis.



the reaction by gas chromatography (GC-FID) and quantify the concentration of product by comparison against an internal standard (dodecane).

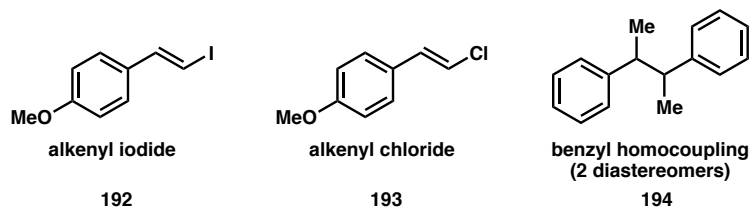
4.4.4.1 Mn and Zn Reductants

Initial investigations revealed that the use of Mn as the reductant resulted in long induction periods (90 minutes) and long reaction times (up to 6 hours). Either activating the Mn with HCl, or using Mn stored under inert atmosphere in the glovebox shortened both the induction period and the reaction time, but only to 30 min and 100 min, respectively. We found that the use of a fine suspension of activated Zn dust began providing the product after a 5–10 min induction period, and the reaction was complete within 40 min. Altering the reductant identity did not significantly affect the overall yield and enantioselectivity of **137**: 96% yield and 96% ee with Mn versus 91% yield and 90% ee with Zn. Doubling the amount of Zn to 6 equivalents increased the reaction rate by a factor of 1.2, results similar to those observed by Weix and coworkers in analogous studies.⁴ We hypothesized that the reduction of Ni(II) by Zn was no longer significantly rate-limiting, allowing us to probe the next rate-determining step in the catalytic cycle.

4.4.4.2 Observation of Side Products

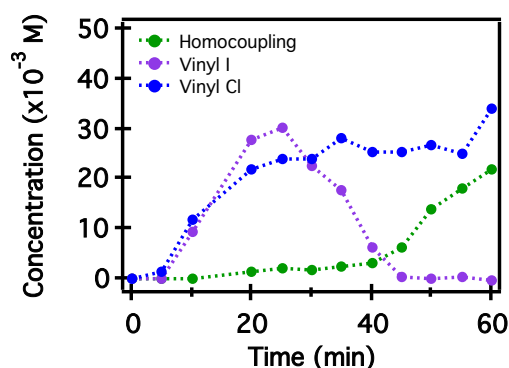
In addition to looking at the concentration of the cross-coupled product over time, we also analyzed the concentration profiles of side products present in the reaction: alkenyl iodide **192**, alkenyl chloride **193**, and benzyl homocoupling **194** (Figure 4.16). Once the induction period terminates, alkenyl iodide and alkenyl chloride are observed in the reaction when monitored by GC (Figure 4.17). Although we observe halide scrambling on the alkenyl C(sp²)-hybridized electrophile, we do not observe halide scrambling on the

Figure 4.16 Side products observed in the catalytic alkenyl–benzyl cross-coupling.



benzylic C(sp³)-hybridized electrophile (no benzyl iodide or benzyl bromide are formed). While alkenyl iodide **192** is a competent electrophile and is consumed by the end of the reaction, alkenyl chloride **193** remains in the reaction mixture. This may explain why the addition of NaI afforded higher reaction yields during the initial reaction optimization⁸—more of the alkenyl electrophile remains a competent electrophile. Furthermore, we also observe the formation of benzyl homocoupling **194** over the course of the reaction. The side product is slowly formed during the reaction, and once full conversion of alkenyl bromide electrophile **86** is achieved, the remaining benzyl chloride **167** rapidly dimerizes.

Figure 4.17 Concentration profiles of side products.

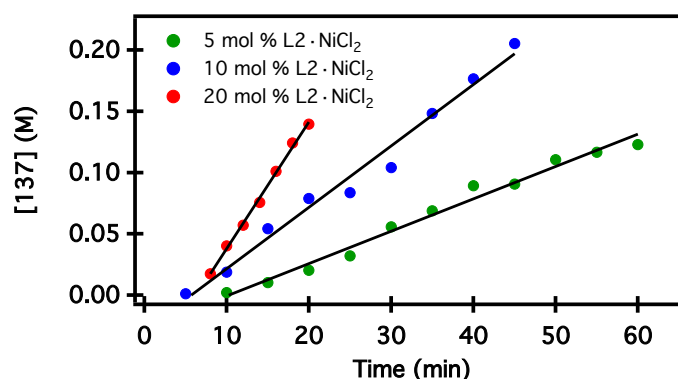


4.4.4.3 Nickel Loading

We then analyzed the observed rate of product formation as a function of reaction time with varying catalyst loadings of L2·NiCl₂. As we sequentially doubled the

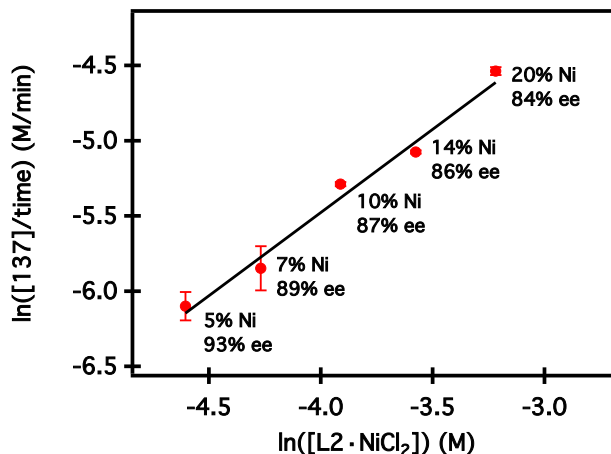
concentration of the catalyst, the observed rate of product formation also doubled (Figure 4.18). After fitting the reaction traces by linear regression, and subsequently graphing the natural log (ln) of the linear slopes versus the ln of the concentration of nickel, we obtained a secondary plot as shown in Figure 4.19. The data points appear to have a linear trend,

Figure 4.18 Concentration of **137** as a function of time at various Ni loadings.



and are best fit by a regression line with an equation of $y = 1.1x - 0.96$ and an R^2 of 0.97. Interestingly the enantioselectivity of the reaction decreases as the concentration of nickel increases. With 5 mol % **L2**·**NiCl₂**, **137** is formed in 93% ee, however with 20 mol % **L2**·**NiCl₂**, **137** is formed in 84% ee. This data suggests that although the reaction appears

Figure 4.19 Rate dependence on Ni loading.

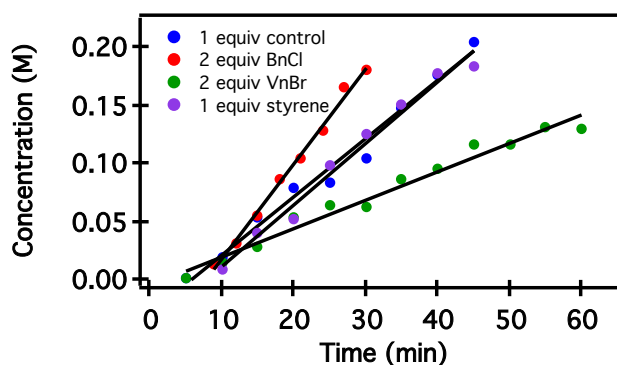


to be first order in nickel for the rate-determining step, there may be a secondary mechanism (with lower enantioselectivity) coexisting with the major pathway at higher catalyst loadings.

4.4.4.4 Electrophile Equivalents

We then analyzed the observed rate of product formation as a function of time when varying the electrophile equivalents (Figure 4.20). With two equivalents of benzyl chloride **167**, the rate of product formation increased by a factor of 1.7. In contrast, when two equivalents of alkenyl bromide **86** were added, the rate of product formation decreased by a factor of 0.5. To determine if the reduction in rate was due to alkenyl bromide coordination to nickel, we added one equivalent of 4-methoxystyrene to the reaction and found no reduction in rate. Therefore, it seems that the inverse dependence due to the alkenyl bromide is not attributable to nickel complexation. These trends are similar to those reported by Weix and co-workers in the reductive cross-coupling of aryl and alkyl iodides.⁴

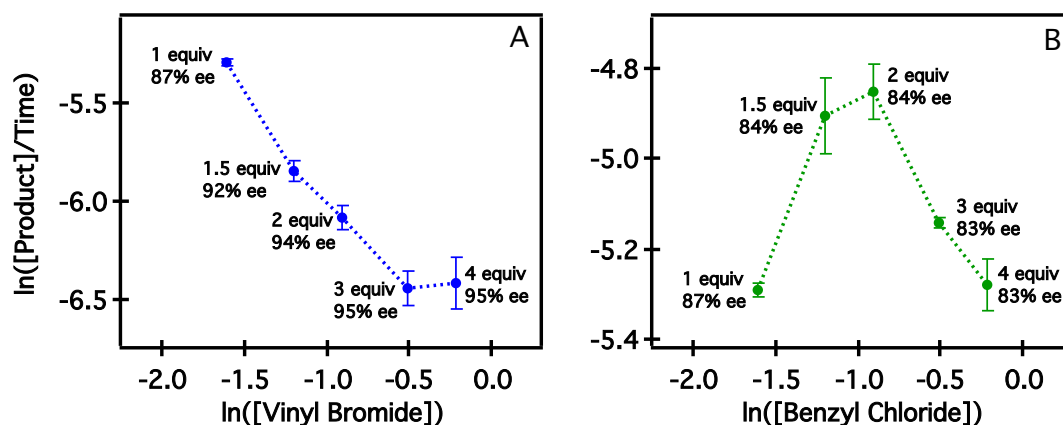
Figure 4.20 Rate of formation of **137** with increased electrophile loadings.



By subjecting the cross-coupling reaction to different equivalents of alkenyl bromide and benzyl chloride, we can generate natural log rate plots. As we increase the concentration of alkenyl bromide **86**, the observed rate of product formation decreases until

it reaches a saturation point at three equivalents (Figure 4.21a). A linear regression line that passes through 1–3 equivalents gives $y = -1.03x - 7.01$ with $R^2 = 0.97$. The enantioselectivity of the reaction also increases as the concentration of **137** increases. With

Figure 4.21 The rate order of A) alkenyl bromide **86** and B) benzyl chloride **167**.

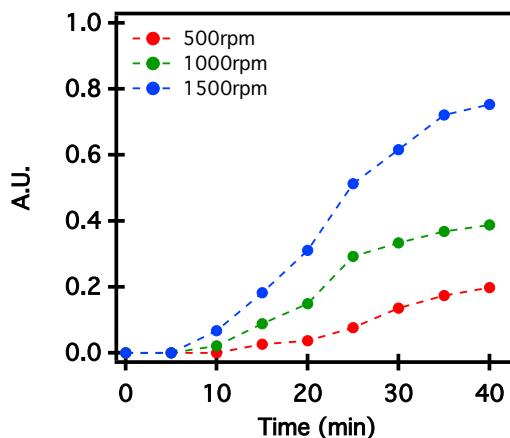


one equivalent of **86**, the product is formed in 87% ee, however with four equivalents of **86**, the product is formed in 95% ee. In contrast, as we increase the concentration of benzyl chloride **167**, the observed rate of product formation increases until two equivalents are added, and then decreases as three and four equivalents are added (Figure 4.21b).

4.4.4.5 Stirring Rate

Lastly, we evaluated the rate of product formation as a function of stir rate; all the previous studies were conducted at 1500 rpm. Figure 4.22 depicts the rate of product formation as the stirring mechanism is altered from 500 rpm to 1000 rpm to 1500 rpm. As the stir speed increases, so does the rate of product formation, which indicates our kinetic studies measure properties related to mass transfer due to the heterogeneous nature of the reaction. As the total surface area of reductant remains constant, increasing the concentration of Ni in solution also increases the number of collisions with the Zn surface.

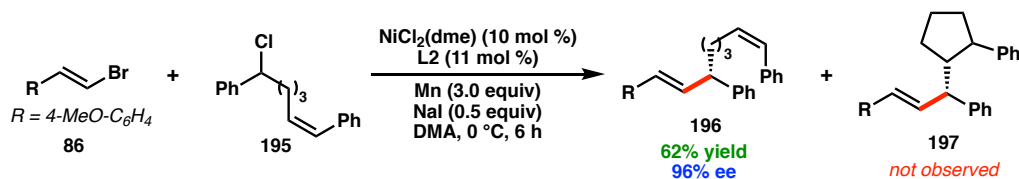
Figure 4.22 Product rate dependence as a function of stir rate.



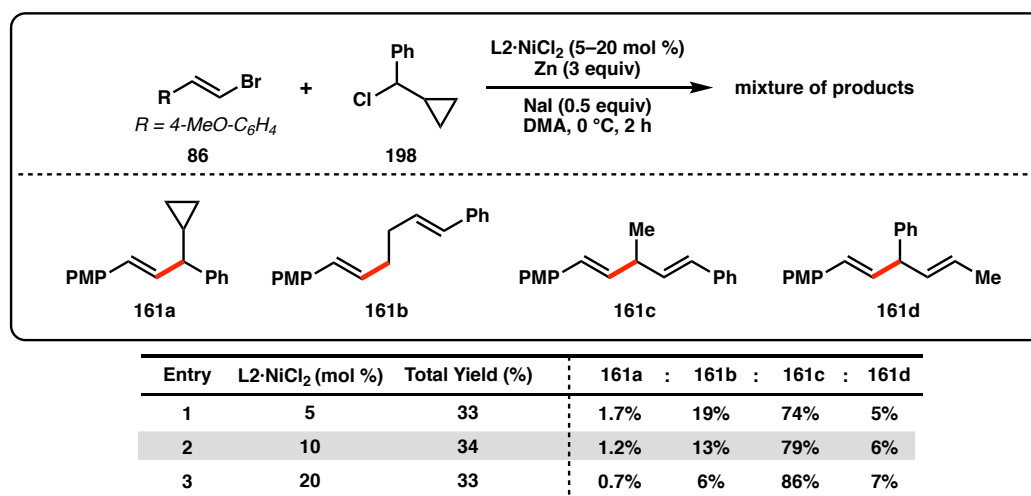
4.4.5 Radical Clock Substrates

To further analyze the probability of a radical intermediate in the mechanism, we synthesized and subjected a series of radical clock substrates to the reaction conditions. When ring closing clock **195** was used as the C(sp³)-hybridized electrophile, a 62% yield of the uncyclized product (**196**) was formed in 96% ee. No ring closed product was observed under the reaction conditions. We then sought to use a faster cyclopropylcarbinyl radical ring opening clock similar to ones employed in our previous studies (Table 4.2).^{10,12,28,29} Unfortunately the stable CF₃-substituted clock did not provide sufficient yield of the coupling products to ensure catalyst turnover;¹² instead a more reactive unsubstituted arene (**198**) had to be prepared. In order to prepare **198**, the benzyl chloride was formed

Scheme 4.8 Evaluation of ring closing clock.



from the corresponding benzyl alcohol using thionyl chloride and immediately used due to its instability. While **198** is stable in DMA at 0 °C for the duration of the reaction (2 h), it is not stable in the presence of other reaction components (i.e. 100% recovery with **Table 4.2**. Evaluation of ring opening clock.



L2·NiCl₂, 60% recovery with Zn, and 50% recovery with NaI). When **198** was subjected to the reaction, we observed a mixture of products (**161a–d**) while the major product observed was the branched ring opening product (**161c**). As the loading of catalyst increased, the ratios of the products changed, however with different trends than observed in our previous studies of NHP esters.¹⁰

4.5 COMPUTATIONAL STUDIES

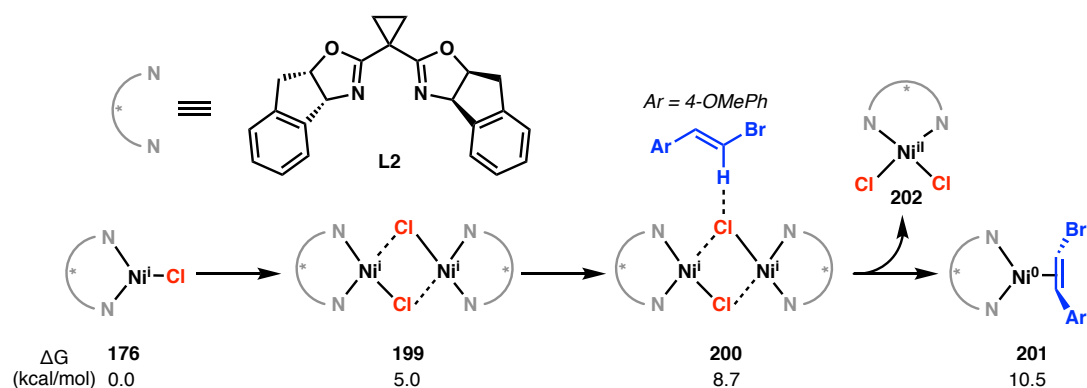
We then sought to conduct computational studies on this transformation. To better understand the differences and compare the likelihood of the intermediate reduction and radical chain mechanisms, we collaborated with Prof. Kendall Houk at UCLA to conduct geometry optimization and energy calculations for the two reaction pathways. Geometry

optimization and frequency analysis were performed using (*E*)-1-(2-bromovinyl)-4-methoxybenzene (**86**), (1-chloroethyl)-benzene (**168**), and chiral bis(oxazoline ligand) **L2** with the B3LYP functional and a mixed basis set of LANL2DZ (for Ni and Br) and 6-31G(d) (for other atoms). Single-point energies were calculated at the M06/6-311+G(d,p) level with SDD for Ni and Br, including the SMD solvation correction (DMA solvent) on the B3LYP-optimized geometries. All calculations were performed with Gaussian 09.

4.5.1 Generation of Ni(0)

Although the generation of Ni(0) in Weix's proposed reaction mechanism (Figure 4.6) is presumed to proceed through a two-electron reduction of Ni(II) via the heterogenous metal reductant, our experimental results suggest that, for **L2**·NiCl₂, only a single electron reduction is viable given the measured reduction potentials of the catalyst. In order to determine an alternate reduction pathway to access Ni(0), we computed the possibility of an alkenyl bromide assisted disproportionation of a Ni(I) dimer **199** (Figure 4.23). Given the energetics of this transformation, it may be a feasible process under the given reaction

Figure 4.23 Evaluation of Ni(I) dimer disproportionation.

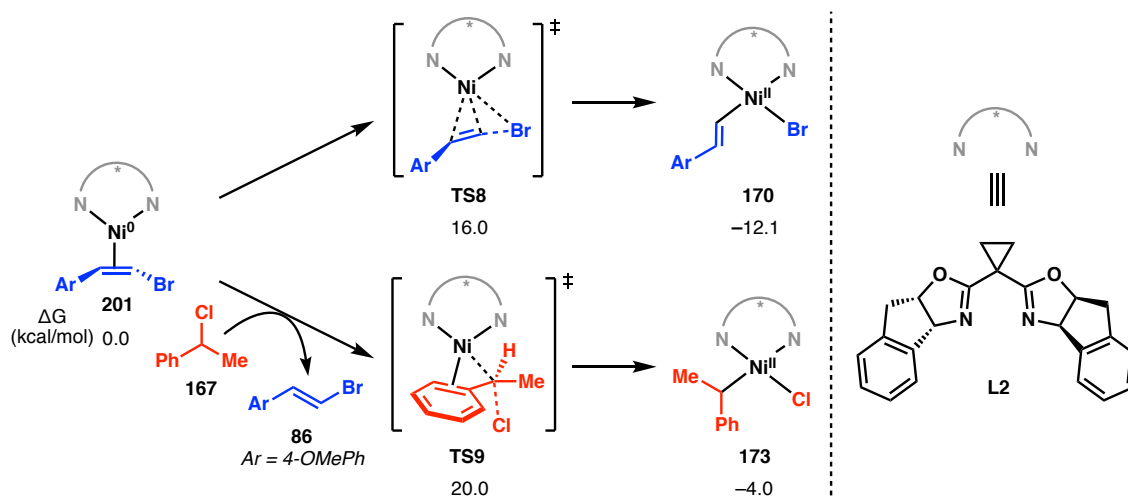


conditions. Further studies aimed at calculating the transition states for this process are ongoing and will shed additional insight into this aspect of the mechanism.

4.5.2 First Oxidative Addition

The first step in both mechanisms is the oxidative addition of alkenyl bromide **86** to Ni(0) complex **169** (Figure 4.24). We first calculated the oxidative addition of alkenyl bromide from a substrate bound Ni(0) complex **201**. Although the oxidative addition of both electrophiles is exergonic ($\Delta G_{\text{rxn}} = -12.1$ kcal/mol for **86** and $\Delta G_{\text{rxn}} = -4.0$ kcal/mol for **167**), comparison of the transition state energies reveals that the oxidative addition of the alkenyl bromide is more favorable by 4.0 kcal/mol ($\Delta G^\ddagger = 16.0$ kcal/mol for **86** and $\Delta G^\ddagger = 20.0$ kcal/mol for **167**). This suggests that given this set of electrophiles, the C(sp²)-hybridized electrophile is the first to undergo oxidative addition to Ni(0) in the catalytic cycle. The oxidative addition of **86** onto Ni(I)Cl complex **176** was also calculated, which was found to be endergonic ($\Delta G_{\text{rxn}} = 13.2$ kcal/mol) with a $\Delta G^\ddagger = 20.2$ kcal/mol.

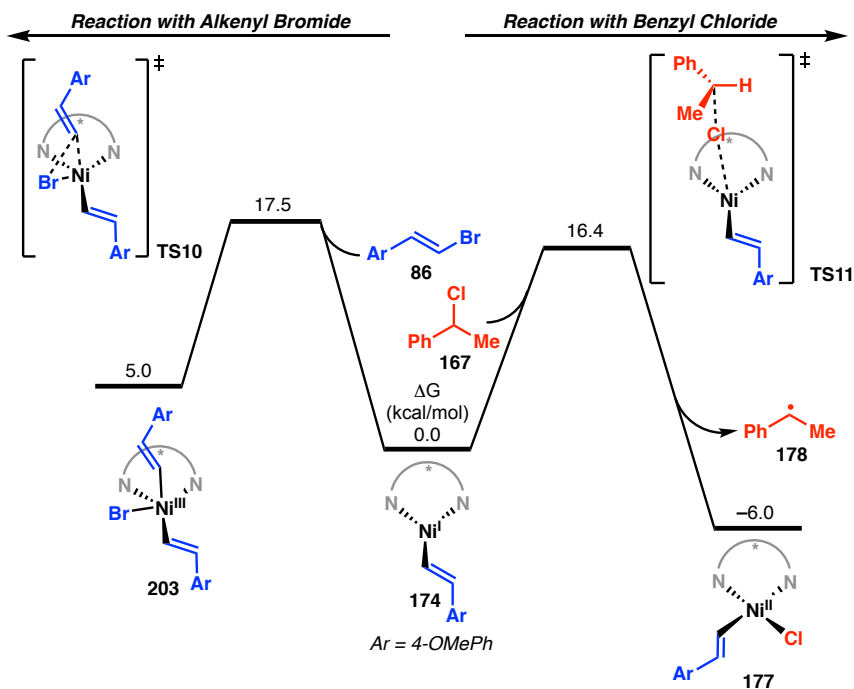
Figure 4.24 Gibbs free energy changes for the oxidative addition pathways of each electrophile to Ni(0) complex **201**.



4.5.3 Preference for Cross-Coupling

From the the Ni(I) alkenyl complex, following reduction of Ni(II) complex **170** by the stoichiometric Mn reductant, we evaluated the oxidative addition of alkenyl bromide **86** through a concerted process and benzyl chloride **167** through a step-wise process which generates an intermediate benzyl radical (Figure 4.25). While the transition state energy for the chloride abstraction by Ni(I) complex **174** and the oxidative addition of alkenyl bromide **86** proceed with a difference of 1.1 kcal/mol, the overall reaction thermodynamics are quite different. Chloride abstraction from the benzyl chloride is exergonic with ΔG_{rxn} of -6.0 kcal/mol. In contrast, oxidative addition of the alkenyl bromide is endergonic with ΔG_{rxn} of 5.0 kcal/mol. These calculations may provide a basis for the high levels of cross-

Figure 4.25 Evaluation of oxidative addition selectivity to $174 \cdot \text{NiR}_{\text{alkenyl}}$. Energies are given in kcal/mol.



electrophile coupling, rather than homocoupling of the alkenyl bromide cross-coupling partner, particularly if the reversible oxidative addition of **86** is favored over reductive elimination to form dienyne homocoupling products.

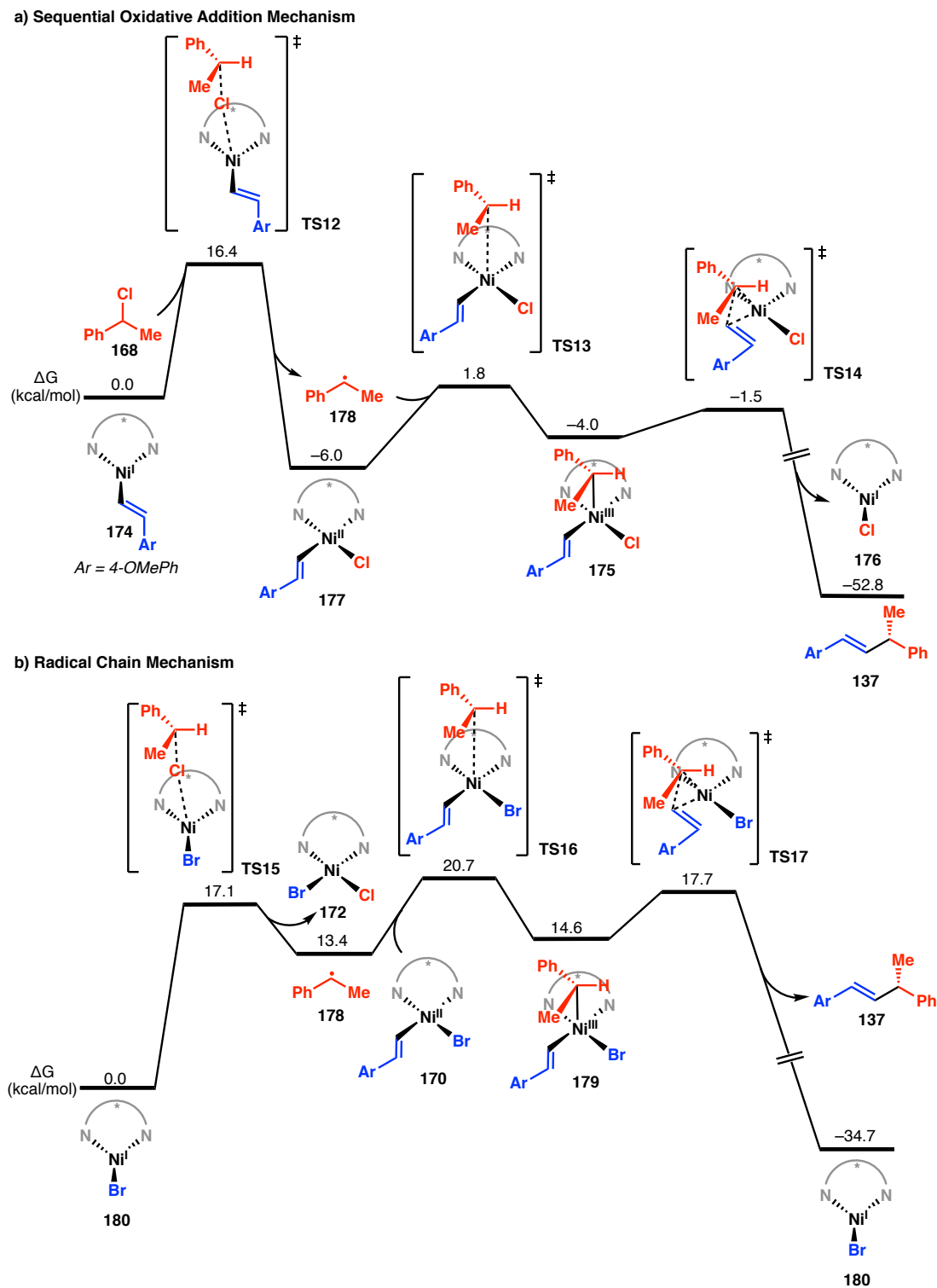
4.5.4 Competing Mechanisms during Second Oxidative Addition

We then calculated the second oxidative addition step of benzyl chloride **168** to Ni(I) complex **174**. As shown in Figure 4.26a, there is a barrier of 16.4 kcal/mol (**TS12**) for the chloride abstraction step in the intermediate reduction mechanism. The resulting benzyl radical **178** attacks Ni(II) complex **177** and forms Ni(III) complex **175**. The cross-coupled product (**137**) is formed following reductive elimination. The radical chain mechanism was also calculated and found to be thermodynamically disfavored by 19.4 kcal/mol (Figure 4.26b). While the chlorine atom transfer step is 6.0 kcal/mol exergonic in the sequential oxidative addition mechanism, it is 13.4 kcal/mol endergonic in the radical chain mechanism. This 19.4 kcal/mol difference leads to the significant preference for the intermediate reduction mechanism.

4.5.5 Alternative Reduction

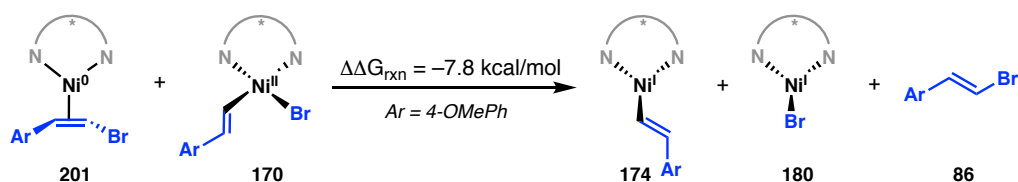
Given our experimental findings that suggest Ni(0) is a competent reductant to reduce $\text{L2} \cdot \text{NiBrR}_{\text{alkenyl}}$ when stoichiometric Ni(cod)₂ is used, we calculated the $\Delta\Delta G_{\text{rxn}}$ for the corresponding comproportionation mechanism between **201** and **170** (Figure 4.27). Alkenyl bromide bound Ni(0) complex **201** and oxidative addition complex **170** are found to form Ni(I) complexes **174** and **180** through a net exergonic reaction, confirming the possibility this process may be feasible. However, under the catalytic reaction conditions, the concentration of Ni(0) in solution is likely very low compared to the amount of

Figure 4.26 Gibbs free energy profile of the benzyl chloride oxidative addition.



heterogeneous reductant available. Aside from kinetic limitations surrounding heterogeneous aspects of the reaction, we speculate that the metal reductant is the most likely source of electrons for the reduction of Ni complex **176**.

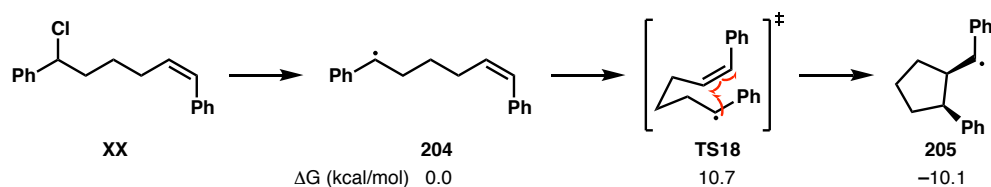
Figure 4.27 Comproportionation to form $L2 \cdot NiR_{vinyl}$.



4.5.6 Radical Clock Substrate

We previously reported the use of benzyl chloride radical clock **195** in our alkenyl–benzyl cross-coupling reaction, however only the uncyclized product was afforded. By calculating the reorganization energy needed for cyclization (Figure 4.28), we determined that a 10.7 kcal/mol barrier is required, which is higher than the 7.8 kcal/mol barrier needed for the addition of benzyl radical **178** to Ni(II) intermediate **170**. Therefore, these studies suggest the radical clock used in the reaction was too slow for cyclization to occur.

Figure 4.28 Calculated Gibbs free energy reorganization energy of the radical cyclization clock.

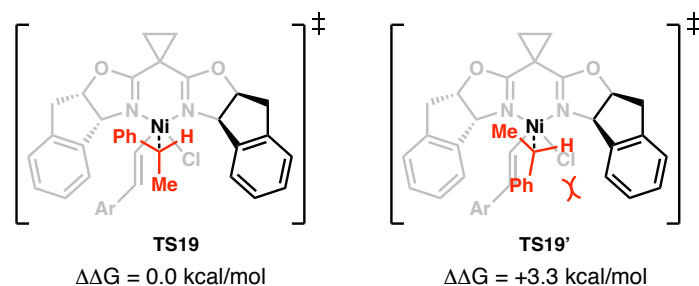


4.5.7 Enantioinduction

The reported cross-coupling reaction not only provides the cross-coupling product **137** in excellent yield (91%) but also in excellent enantioselectivity (93% ee). The

calculated reaction profile (Figure 4.26a) identifies the addition of benzyl radical **178** to Ni(II) intermediate **177** as the enantiodetermining step ($\Delta\Delta G^\ddagger = 3.3$ kcal/mol between reversible benzyl radical addition and reductive elimination). To explore the origins of enantioinduction, the structures and relative Gibbs free energies of the competing transition states for radical addition were computed (Figure 4.29).

Figure 4.29 Relative Gibbs free energy of the transition states for the enantiodetermining step.



In both transition states, the smallest substituent of the approaching benzyl radical, hydrogen, is pointing towards the bulky indanyl group on the ligand. This allows the largest substituent, the phenyl group, to project away from the bulky region of the ligand in the favored transition state **TS19**. In the disfavored transition state, **TS19'**, the phenyl group is proximal to the bulky region of the ligand. This results in an almost perfectly staggered approach of the benzyl radical with respect to the Ni ligands in **TS19**, while steric repulsion from the ligand forces the benzyl radical to adopt a more eclipsed conformation in **TS19'**.

The free energy difference between **TS19** and **TS19'** is computed to be 3.3 kcal/mol, which suggests the reaction should proceed with a 547 ratio of major to minor enantiomers according to Equation 4, or an enantioselectivity of 99.8% ee. However, the computed $\Delta\Delta G^\ddagger$ overestimates the ee of the reaction. One possible explanation for the

overcompensation of ee may be due to competing mechanisms in the reaction, whereby background reactivity accounts via a racemic or less selective pathway accounts for the diminished ee. Nevertheless, **TS19** does lead to the formation of the major enantiomer and is consistent with the observed enantioselectivity. This stereochemical model also provides insight as to why a variety of alkyl substituents are tolerated at the benzylic position, since it projects the medium sized group away from the metal/ligand framework.

$$\frac{x_{major}}{x_{minor}} = 10^{\frac{\Delta\Delta G^\ddagger}{T \times (1.98 \times 10^{-3}) \times 2.3}} \quad (4)$$

The free energy difference between the major and minor transition states for a series of substituted benzylic chlorides was calculated (Table 4.3). Equation 4 can be rearranged to form Equation 5, allowing for experimental $\Delta\Delta G^\ddagger$ values to be determined from the ratio of major and minor enantiomers used in the calculation of %ee. The calculated $\Delta\Delta G^\ddagger$ values

$$\Delta\Delta G^\ddagger = T \times (1.98 \times 10^{-3}) \times 2.3 \times \log_{10} \left(\frac{x_{major}}{x_{minor}} \right) \quad (5)$$

for an α -ethyl group are larger than the values calculated for an α -methyl group, which is consistent with the observed results (entries 1–2). However, when evaluating different aryl

Table 4.3. Evaluation of $\Delta\Delta G^\ddagger$ from major and minor transition states.

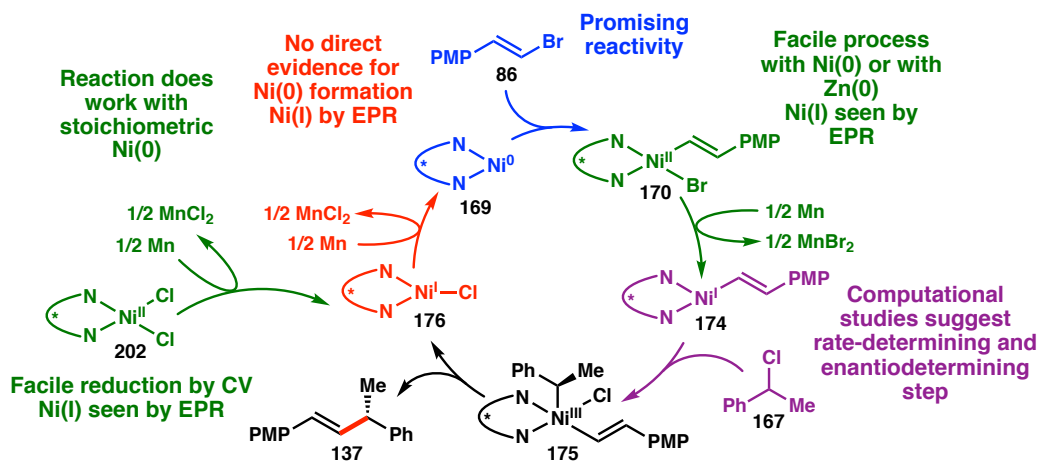
Entry	Ar	R	ee (%) <i>experimental</i>	$\Delta\Delta G$ (kcal/mol) <i>experimental</i>	$\Delta\Delta G$ (kcal/mol) <i>computational</i>
1	Ph	Me	96	2.1	3.3
2	Ph	Et	97	2.3	4.3
3	4-OMePh	Me	93	1.8	3.2
4	4-ClPh	Me	88	1.5	3.4

substituents, the trend is unclear. Both an electron-donating group (OMe, entry 3) and an electron-withdrawing group (Cl, entry 4) were found to decrease the experimental $\Delta\Delta G^\ddagger$ however only the methoxy substituent was found to decrease the calculated $\Delta\Delta G^\ddagger$. The calculated $\Delta\Delta G^\ddagger$ for the chloride substituent was found to be higher than the parent compound. Further studies are ongoing to probe the $\Delta\Delta G^\ddagger$ for additional substrates.

4.6 CONCLUSIONS AND FUTURE DIRECTIONS

In summary, we have conducted a variety of experiments to probe the mechanism of the asymmetric Ni-catalyzed reductive cross-coupling of alkenyl bromides and benzyl chlorides. A series of stoichiometric nickel studies probed each step in the catalytic cycle (Figure 4.30). The $L2 \cdot NiCl_2$ complex reduces to afford $L2 \cdot NiCl$ complex as determined by CV and EPR, however there is no evidence for the direct reduction of Ni(I) to form $L2 \cdot Ni(0)$ in DMA under the reactions conditions. The cross-coupling reaction does proceed to afford **137** with high levels of enantioselectivity when stoichiometric $Ni(cod)_2$

Figure 4.30 Evidence supporting sequential oxidative addition mechanism.

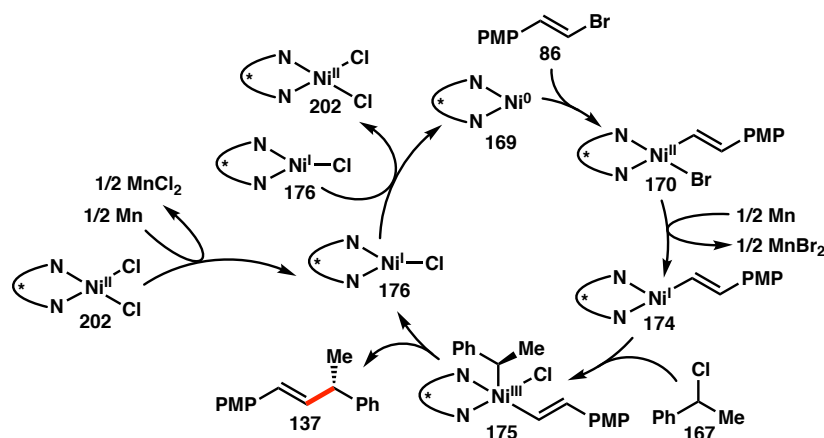


is used, and analysis by EPR further demonstrates the feasibility of both a Ni(0) and Zn mediated reduction of $L2 \cdot NiBrR_{alkenyl}$.

Computational studies suggest that the intermediate reduction mechanism is favored over the radical chain mechanism by $\Delta\Delta G_{rxn}$ of 19.4 kcal/mol in the chlorine atom transfer step. Comparison of the highest barrier between the two mechanisms shows sequential oxidative addition mechanism is lower by 4.3 kcal/mol. These computational studies also suggest that a Ni(I) dimer could potentially undergo a disproportionation reaction to afford a Ni(II) species as well as the requisite Ni(0) needed for oxidative addition of the alkenyl bromide electrophile. An updated mechanistic understanding including this process is depicted in Figure 4.31.

Future studies are needed to obtain a better understanding of the speciation of Ni following reduction of $L2 \cdot NiCl_2$ by Zn. In addition, the isolation and characterization of oxidative addition complexes would prove valuable to this study. Additional kinetic analysis on a homogeneous variant of the reaction (NHP esters with TDAE) may shed additional insight into the rate-limiting step of the reaction and help identify the resting

Figure 4.31 Hypothesis on reaction mechanism.



state of the catalyst. Finally, additional computational studies would provide valuable insight into chemoselectivity of the proposed mechanism. Currently, the addition of alkenyl bromide decreases the rate of product formation when Zn is used as a heterogeneous reductant. Additional computational studies aimed at identifying the energetics of the pathway for the formation of alkenyl dimer, as well as both alkenyl bromide and benzyl chloride oxidative addition and subsequent elimination from a Ni(I)-benzyl complex would be insightful.

It is often said that a mechanism can never be proven, it can only be disproven.³⁰ While concrete, irrefutable data to pin down the reaction mechanism is not yet obtained (if such is even possible), these studies highlight the difficulties and challenges associated with mechanistic studies of asymmetric Ni catalysis occurring in heterogeneous systems. Nevertheless, we predict that future studies on the mechanisms of Ni-catalyzed reductive cross-couplings will not only shed insight into previously developed reactions, but also serve as a basis to develop new reactions and enrich the field of organic synthesis.

4.7 EXPERIMENTAL SECTION

4.7.1 Materials and Methods

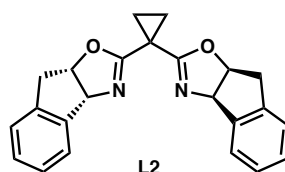
Unless otherwise stated, reactions were performed under a nitrogen atmosphere using freshly dried solvents. Tetrahydrofuran (THF) was dried by passing through activated alumina columns. Anhydrous *N,N*-dimethylacetamide (DMA) was purchased from Aldrich and stored under inert atmosphere. Manganese powder (~325 mesh, 99.3%) was purchased from Alfa Aesar. Zinc dust (97.5%) was purchased from Strem. Unless otherwise stated,

chemicals and reagents were used as received. All reactions were monitored by thin layer chromatography using EMD/Merck silica gel 60 F254 pre-coated plates (0.25 mm) and were visualized by UV, CAM, or KMnO₄ staining. Flash column chromatography was performed as described by Still et al.³¹ using silica gel (particle size 0.032–0.063) purchased from Silicycle. Optical rotations were measured on a Jasco P-2000 polarimeter using a 100 mm path-length cell at 589 nm. ¹H and ¹³C NMR spectra were recorded on a Varian Inova 300 (at 300 MHz and 75 MHz, respectively), Varian 400 MR (at 400 MHz and 101 MHz, respectively) or a Varian Inova 500 (at 500 MHz and 126 MHz, respectively), and are reported relative to internal chloroform (¹H, δ = 7.26, ¹³C, δ = 77.0). ¹⁹F NMR spectra were recorded on a Varian 400 MR (at 376 MHz). Data for ¹H NMR spectra are reported as follows: chemical shift (δ ppm) (multiplicity, coupling constant (Hz), integration). Multiplicity and qualifier abbreviations are as follows: s = singlet, d = doublet, t = triplet, q = quartet, p = pentet, m = multiplet, br = broad. IR spectra were recorded on a Perkin Elmer Paragon 1000 spectrometer and are reported in frequency of absorption (cm⁻¹). Analytical chiral SFC was performed with a Mettler SFC supercritical CO₂ analytical chromatography system with Chiralcel AD-H, OD-H, AS-H, OB-H, and OJ-H columns (4.6 mm x 25 cm). Analytical achiral GC was performed with an Agilent 6850 GC utilizing an HP-1 capillary column (methyl siloxane, 30.0 m x 320 μm x 0.25 μm, Agilent) column with a splitless injection and a helium flow of 7.3 mL/min. The temperature program began at 50 °C and was held for 2 min, increased to 250 °C at 25 °C/min and then held at 250 °C for 3 min. X-band EPR spectra were recorded on a Bruker EMX spectrometer. Electrochemical measurements were conducted under an N₂

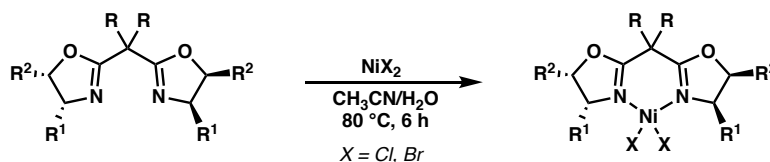
atmosphere in a one compartment cell using a Bio-Logic SP300 potentiostat/galvanostat. A glassy carbon disk working electrode, silver wire pseudo-reference electrode, and graphite auxiliary electrode were used. Electronic absorbance spectra were recorded with a Varian Cary Bio 50 spectrophotometer.

4.7.2 Nickel(II) Complex Preparation

For the synthesis of ligand **L2**, see Chapter 2.



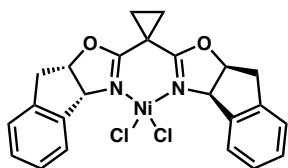
General Procedure 1: $L \cdot NiX_2$ Complex Synthesis



Similar to a procedure reported by Evans and co-workers,³² the bis(oxazoline) ligand (1.2 mmol, 1 equiv) and either anhydrous nickel(II) chloride (1.2 mmol, 1 equiv) or anhydrous nickel(II) bromide (1.2 mmol, 1 equiv) were added to a round bottom flask equipped with a magnetic stirring rod and dissolved in a mixture of MeCN (26 mL) and water (340 μ L). The solution was heated to 80 °C for 6 hours to afford a dark purple solution. The reaction was concentrated under reduced pressure and the obtained solid was recrystallized by vapor diffusion (DCM/pentanes) to afford crystals suitable for X-ray diffraction. For quantitative isolation of $L \cdot NiX_2$, hexanes was vigorously added by pipet to suspend any residual solid that had not crystallized, and then was subsequently removed. The washed crystals were

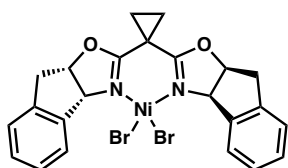
then removed with a spatula, transferred to a new vial, and crushed to provide a fine powder. The resulting complex was dried under vacuum to afford the desired product.

Nickel(II) bis(chloride) (3a*R*,3a'*R*,8a*S*,8a'*S*)-2,2'-(cyclopropane-1,1-diyl)bis(3a,8a-dihydro-8*H*-indeno[1,2-*d*]oxazole) (L2·NiCl₂)



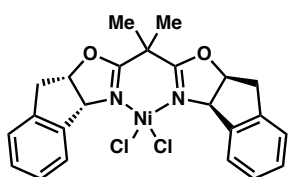
Prepared from bis(oxazoline) **L2** (428 mg, 1.2 mmol) and nickel(II) chloride (156 mg, 24 mmol) following General Procedure 1. The crude residue was recrystallized by vapor diffusion (DCM/pentane) to yield purple crystals of **L2·NiCl₂** as the monomeric complex. See Chapter 2 for characterization.

Nickel(II) bis(bromide) (3a*R*,3a'*R*,8a*S*,8a'*S*)-2,2'-(cyclopropane-1,1-diyl)bis(3a,8a-dihydro-8*H*-indeno[1,2-*d*]oxazole) (L2·NiBr₂)



Prepared from bis(oxazoline) **L2** (73 mg, 0.2 mmol) and nickel(II) bromide (45 mg, 0.2 mmol) following General Procedure 1. The crude residue was recrystallized by vapor diffusion (DCM/pentane) to yield purple crystals of **L2·NiBr₂** as the monomeric complex. See Chapter 3 for characterization.

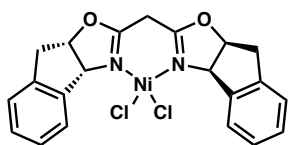
Nickel(II) bis(chloride) (3a*R*,3a'*R*,8a*S*,8a'*S*)-2,2'-(propane-2,2-diyl)bis(3a,8a-dihydro-8*H*-indeno[1,2-*d*]oxazole) (L9·NiCl₂)



Prepared from bis(oxazoline) **L9** (71 mg, 0.2 mmol) and nickel(II) chloride (26 mg, 0.2 mmol) following General Procedure 1. The crude residue was recrystallized by vapor diffusion

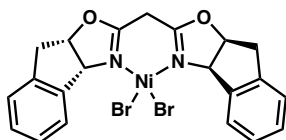
(DCM/pentane) to yield orange crystals of **L9·NiCl₂** as the chloride bridged trimer complex.

Nickel(II) bis(chloride) bis((3*aR*,8*aS*)-3*a*,8*a*-dihydro-8*H*-indeno[1,2-*d*]oxazol-2-yl)methane (L20·NiCl₂)



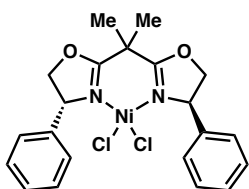
Prepared from bis(oxazoline) **L20** (66 mg, 0.2 mmol) and nickel(II) chloride (26 mg, 0.2 mmol) following General Procedure 1. The crude residue was recrystallized by vapor diffusion (DCM/pentane) to yield orange crystals of **L20·NiCl₂** as the chloride bridged trimer complex.

Nickel(II) bis(bromide) bis((3*aR*,8*aS*)-3*a*,8*a*-dihydro-8*H*-indeno[1,2-*d*]oxazol-2-yl)methane (L20·NiBr₂)



Prepared from bis(oxazoline) **L20** (66 mg, 0.2 mmol) and nickel(II) bromide (45 mg, 0.2 mmol) following General Procedure 1. The crude residue was recrystallized by vapor diffusion (CH₂Cl₂/pentane) to yield orange crystals of **L20·NiBr₂** as the bromide bridged trimer complex.

Nickel(II) bis(chloride) ((4*R*,4'*R*)-2,2'-(propane-2,2-diyl)bis(4-phenyl-4,5-dihydrooxazole) (L1·NiCl₂)



Prepared from bis(oxazoline) **L1** (67 mg, 0.2 mmol) and nickel(II) chloride (26 mg, 0.2 mmol) following General Procedure 1. The crude residue was recrystallized from DCM/pentane by slow

evaporation to yield green crystals of **L1**·NiCl₂ as the hydrated chloride bridged dimer complex.

4.7.3 Electronic Absorption

A series of 20 mL scintillation vials were charged with the **L2**·NiCl₂ complex (4.4 – 5.0 mg) and desired solvent (5 mL of CH₂Cl₂, MeCN, acetone, EtOAc, DMA, NMP, DMF, DMPU, DMSO, or water). The solutions were analyzed with a UV/Visible spectrometer after collecting blank samples of each solvent. Absorbance data was converted to extinction coefficients (M⁻¹ cm⁻¹) by using the measured mass, volume of solvent, and the path length of the quartz cuvette (1 cm).

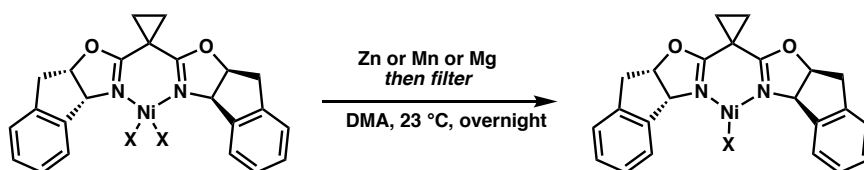
4.7.4 Cyclic Voltammetry

A 20 mL scintillation vial was charged with the **L2**·NiCl₂ complex (5.9 mg, 0.012 mmol) and Bu₄NPF₆ (387.6 mg, 10 mmol). Then anhydrous DMA (10 mL) was added and the solution was stirred to ensure homogeneity. The final concentration of each compound was 1.2 mM **L2**·NiCl₂ and 0.1 M Bu₄NPF₆. To a second 20 mL scintillation vial was added **L2**·NiCl₂ (10.2 mg, 0.021 mmol), ferrocene (3.8 mg, 0.02 mmol), and Bu₄NPF₆ (774.9 mg, 20 mmol). Then anhydrous DMA (20 mL) was added and the solution was stirred to ensure homogeneity. The final concentration of each compound was 1.1 mM **L2**·NiCl₂, 1 mM ferrocene, and 0.1 M Bu₄NPF₆. A three electrode cell with a glassy carbon disk working electrode, a silver wire pseudo-reference electrode, and a graphite rod auxiliary electrode was connected to the potentiostat and the electrodes were placed in the solution. Cyclic voltammetry was used to determine the reduction potential of **L2**·NiCl₂ while scanning at

a rate of 0.1 V/s against the Ag wire reference electrode. The potential was normalized by setting the Fc/Fc⁺ redox couple to 0.0 V.

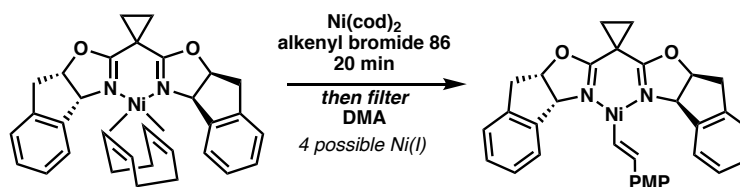
4.7.5 EPR Spectroscopy

EPR of L2·NiX Complexes



To a 2 dram vial in the glovebox was added L2·NiCl₂ or L2·NiBr₂ (0.01–0.10 mmol, 1 equiv), the metal reductant (0.1–1.0 mmol, 10 equiv), and anhydrous DMA (1 mL). The solution was stirred at room temperature overnight to produce a dark orange solution. The reaction mixture was filtered through a Kimwipe plug in a glass pipet to remove excess reductant, added to a quartz EPR tube, and sealed. The sample was brought out of the glovebox and immediately frozen in liquid nitrogen. EPR spectra were collected at 77 K. EPR simulations of 0.01 mM L2·NiCl were conducted using EasySpin in MATLAB. The simulated parameters were defined as follows: g_1 : 2.4879, g_2 : 2.1588, g_3 : 2.1092, A_{Cl} : 1.2 MHz, Line Width: 4.4773, Microwave Frequency: 9.5 GHz, Range: 1000 G - 4000 G, Temperature: 77 K, RMSD: 0.0288.

EPR of L2·NiR_{alkenyl} from Ni(cod)₂



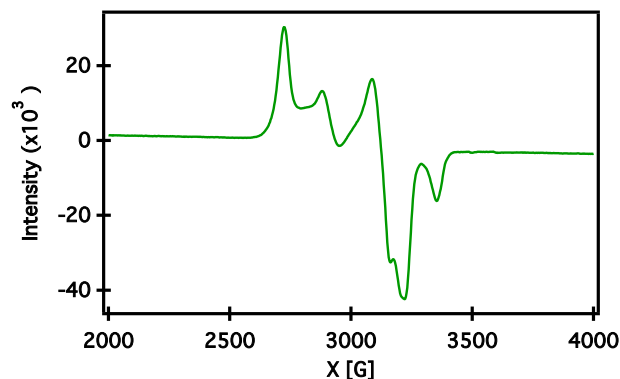
The Ni(cod)₂ (5.6 mg, 0.02 mmol, 2 equiv) and bis(oxazoline) ligand **L2** (3.7 mg, 0.01 mmol, 1 equiv) were added to a 2 dram vial in the glovebox and dissolved in DMA (1 mL). The solution was stirred for 14 hours and turned an orange-red color. The alkenyl bromide **86** (2.2 mg, 0.01 mmol, 1 equiv) was added and stirred for 20 minutes before being filtered through a Kimwipe plug in a glass pipet. The solution was added to a quartz EPR tube, sealed, brought out of the glovebox, and immediately frozen in liquid nitrogen. EPR spectra were collected at 77 K. Upon continued stirring (> 1 day), the solution turned purple, plated out Ni⁰, contained no Ni(I) signal by EPR, and alkenyl dimer was detected by GCMS.

EPR of L2·NiR_{alkenyl} complex from L2·NiCl₂

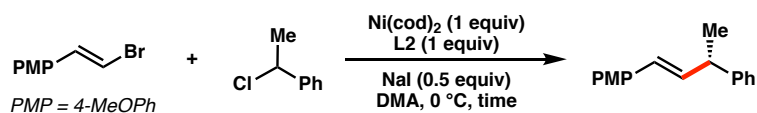


The L2·NiCl₂ complex (4.7 mg, 0.01 mmol, 1 equiv) and zinc dust (6.9 mg, 0.1 mmol, 10 equiv) were added to a 2 dram vial in the glovebox and dissolved in DMA (1 mL). The solution was stirred for 10 minutes. The alkenyl bromide **86** (2.2 mg, 0.01 mmol, 1 equiv) was added and stirred for an additional 20 minutes before being filtered through a Kimwipe plug in a glass pipet. The solution was added to a quartz EPR tube, sealed, brought out of the glovebox, and immediately frozen in liquid nitrogen. EPR spectra were collected at 77 K. Upon continued stirring (> 1 day), the solution turned a brown/orange, contained trace Ni(I) signal by EPR, and alkenyl dimer was visible by GC-MS analysis.

Figure 4.32 EPR spectra of $L2 \cdot NiCl_2$ reduction in the presence of alkenyl bromide.

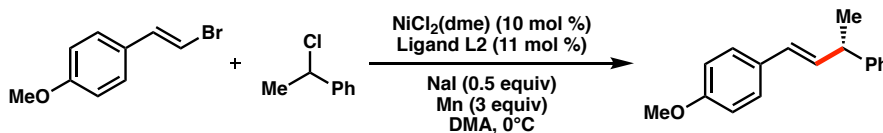


4.7.6 Stoichiometric Ni(0) Studies



To a 10 mL round bottom flask (6 h reactions) or a 20 mL scintillation vial (24 h reactions) equipped with a magnetic stir bar was added alkenyl bromide **86** (42.9 mg, 0.2 mmol, 1 equiv), NaI (15.4 mg, 0.1 mmol, 0.5 equiv), and ligand **L2** (71.7 mg, 0.2 mmol, 1 equiv). The vial was brought into the glovebox and the Ni(cod)₂ (55.4 mg, 0.2 mmol, 1 equiv) was added followed by 2 mL of anhydrous DMA. The reaction was cooled to 0 °C before benzyl chloride **167** (26 μL, 0.2 mmol, 1 equiv) was added. The reaction was warmed to room temperature before an internal standard (25 μL benzyl ether) was added. The reaction was quenched with 5 mL of 1 M HCl followed by 5 mL of water. The organic material was extracted with diethyl ether (3 x 10 mL), washed with brine (10 mL) and dried with MgSO₄ before being filtered and concentrated. The crude mixture was analyzed by ¹H NMR and chiral SFC to obtain the product yield and ee.

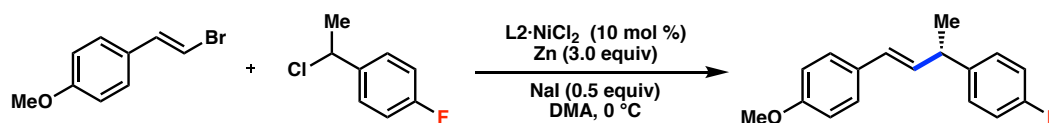
4.7.7 Scalemic Ligand Study



The reaction was conducted under the reported reaction conditions,⁸ however a mixture of the two enantiomers of the ligand was made to conduct the reaction with scalemic ligand. The ee of the ligand used was 0, 15, 30, 50, 75, 90, and 100% ee. The measured % ee of the product was graphed as a function of the % ee of the ligand to give a linear trend of $y = 0.90x - 0.99$ with an $R^2 = 0.99$.

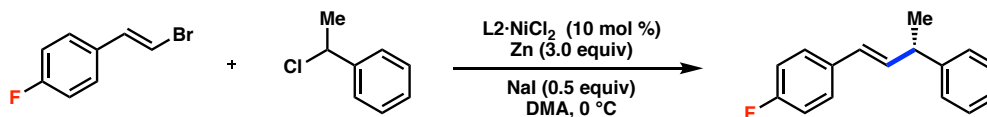
4.7.8 Analysis of Reaction by ^{19}F NMR

Benzyl Chloride ^{19}F Label



The reaction was conducted as described in literature with the exception of Zn as the reductant.⁸ A fluorine tag was incorporated on the benzyl chloride electrophile. The reaction products were monitored by ^{19}F NMR over the course of the reaction by analyzing aliquots with C_6F_6 as an internal standard.

Alkenyl Bromide ^{19}F Label



The reaction was conducted as described in literature with the exception of Zn as the reductant.⁸ A fluorine tag was incorporated on the alkenyl bromide electrophile. The reaction products were monitored by ¹⁹F NMR over the course of the reaction by analyzing aliquots with C₆F₆ as an internal standard.

4.7.9 Kinetics Procedures, Standards, and GC-FID Fits

Standard Reaction with Zinc Powder

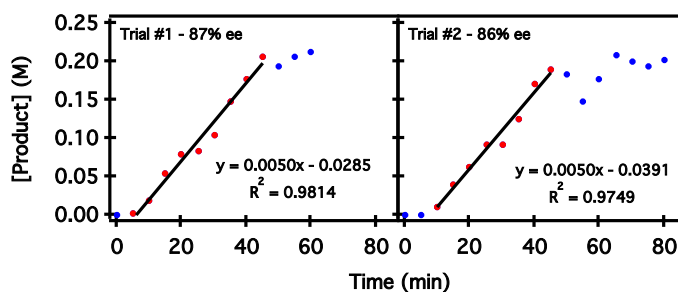


A 10 mL round bottom flask with a small magnetic stirring rod was charged with the sodium iodide (22.5 mg, 0.15 mmol, 0.5 equiv) and zinc dust (58.8 mg, 0.9 mmol, 3 equiv). The flask was sealed with a rubber septum, purged with N₂, and cooled to 0 °C by being placed in an ice water bath. Alkenyl bromide **86** (85.2 mg, 0.4 mmol) and L2·NiCl₂ (19.4 mg, 0.04 mmol) were added to a 2 mL volumetric flask, sealed with a rubber septum, and purged with N₂. Benzyl chloride **167** (53 μL, 0.4 mmol) and dodecane (48 μL) as an internal standard were added via syringe to the volumetric flask. Then anhydrous DMA was added to the volumetric flask until it reached the 2 mL line. A small stir bar was added to the volumetric flask and the solution was stirred until all of the reagents dissolved. The solution was taken up into a 2 mL syringe to ensure homogeneity, and then 1.5 mL of the solution was added to the round bottom flask. The reaction was stirred under a positive N₂ flow by using an IKA stir plate set to a stirring speed of 1500 rpm. At appropriate time points, approximately 50 μL of the solution was removed by syringe (syringe and needle

were pre-flushed with N₂), loaded onto a short silica plug (1 cm) in a glass pipette packed with cotton. The crude mixture was flushed through the silica plug with 2 mL of 10% EtOAc/hexane directly into GC vials and analyzed by GC-FID. Upon the completion of data collection, the remaining volume of the reaction in the round bottom flask was also analyzed by chiral phase SFC to obtain the enantioselectivity (% ee) of the cross-coupled product.

All data runs obtained from the GC-FID instrument were appropriately integrated for the product and the dodecane standard. The integrated data points were further processed by normalizing each product area value by its corresponding standard area value. The normalized areas were then converted to concentration by using calculated response factors obtained from preparing known mixtures of the standard and purified reaction product. Each reaction was analyzed and graphed to show the product concentration (M) as a function of reaction time (min). All data points were plotted with blue markers (•) as shown below, while only the data points included in the linear fit are shown with red markers (•). The best-fit linear regression line is also shown and the $y=mx+b$ equation is given. Each reaction was run in duplicates as indicated by Trial 1 and Trial 2.

Figure 4.33 Standard reaction conditions.



Effect of Changing Ni Loading

The standard reaction procedure was followed, except varying amounts of **L2**·NiCl₂ were added to give final loadings of 5%, 7%, 14%, and 20% nickel.

Figure 4.34 Reaction conditions with 5% **L2**·NiCl₂.

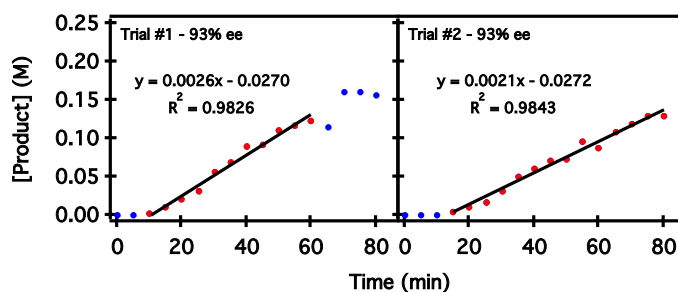


Figure 4.35 Reaction conditions with 7% **L2**·NiCl₂.

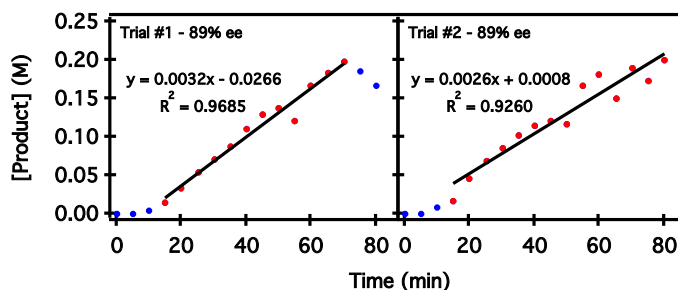


Figure 4.36 Reaction conditions with 14% **L2**·NiCl₂.

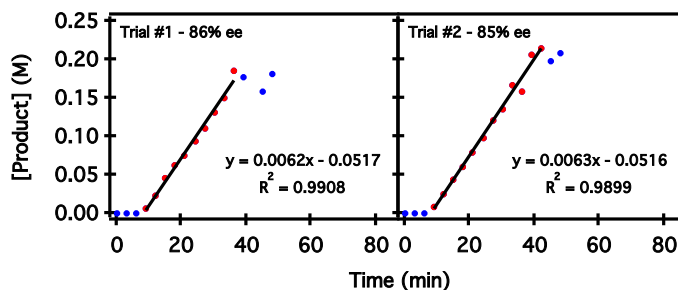
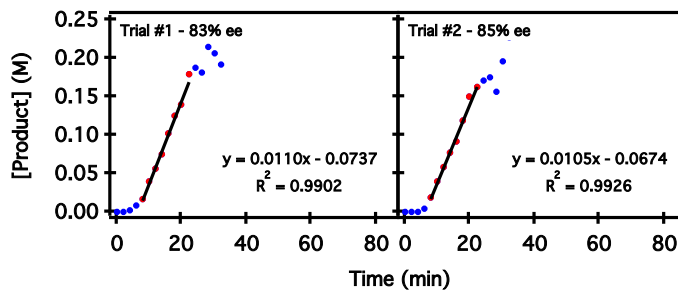


Figure 4.37 Reaction conditions with 20% **L2**·NiCl₂.



4.7.9.1 Effect of Changing Alkenyl Bromide Equivalents

The general reaction procedure was followed, except varying amounts of alkenyl bromide **86** were added to give final amounts of 1.5, 2, 3, and 4 equivalents.

Figure 4.38 Reaction conditions with 1.5 equivalents of alkenyl bromide **86**.

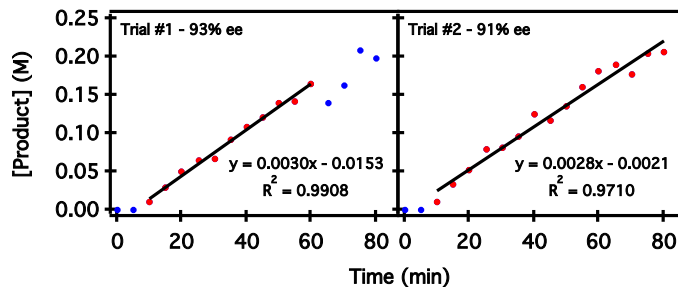


Figure 4.39 Reaction conditions with 2.0 equivalents of alkenyl bromide **86**.

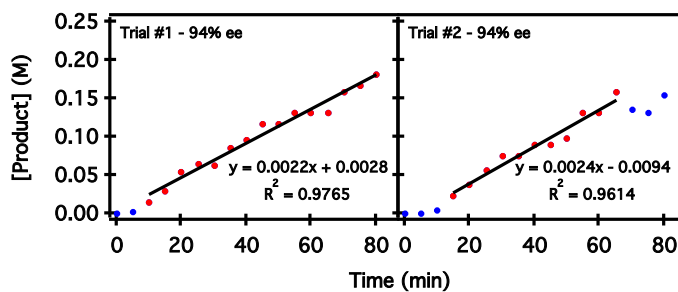


Figure 4.40 Reaction conditions with 3.0 equivalents of alkenyl bromide **86**.

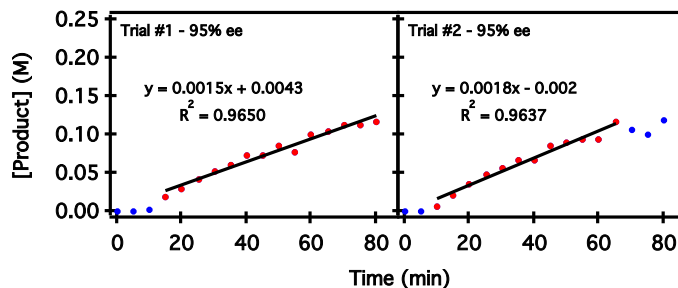
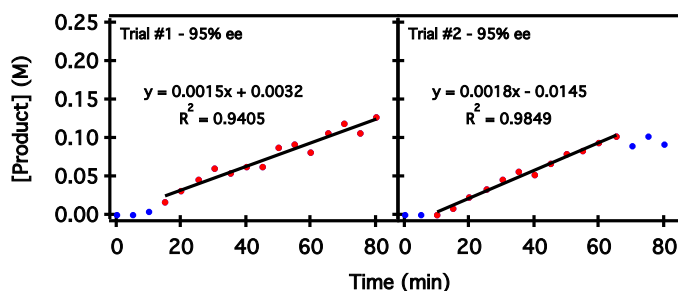


Figure 4.41 Reaction conditions with 4.0 equivalents of alkenyl bromide **86**.



Effect of Changing Benzyl Chloride Equivalents

The general reaction procedure was followed, except varying amounts of benzyl chloride **167** were added to give final amounts of 1.5, 2, 3, and 4 equivalents.

Figure 4.42 Reaction conditions with 1.5 equivalents of benzyl chloride **167**.

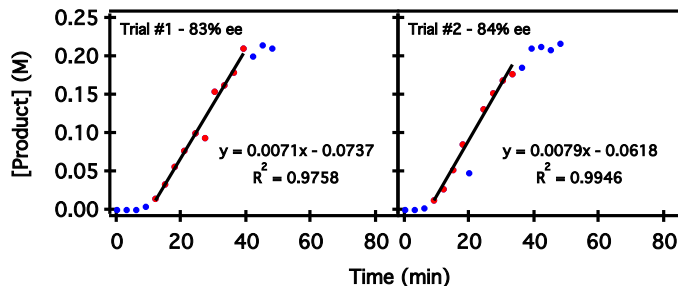


Figure 4.43 Reaction conditions with 2.0 equivalents of benzyl chloride **167**.

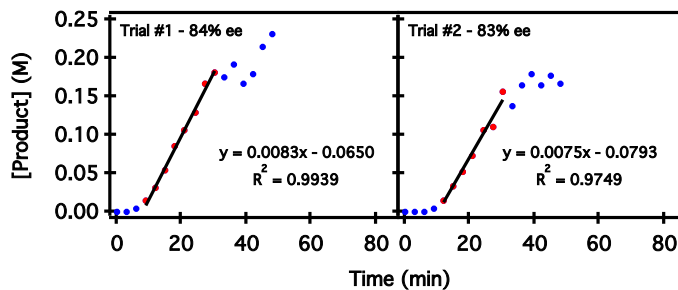


Figure 4.44 Reaction conditions with 3.0 equivalents of benzyl chloride **167**.

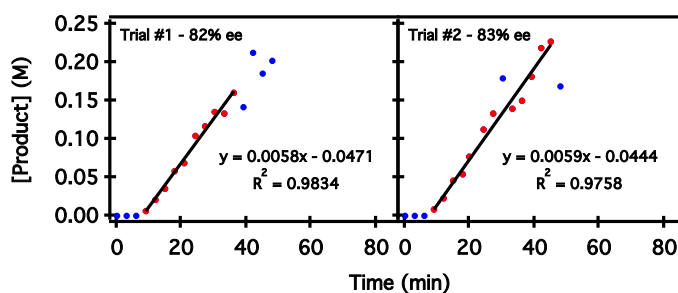
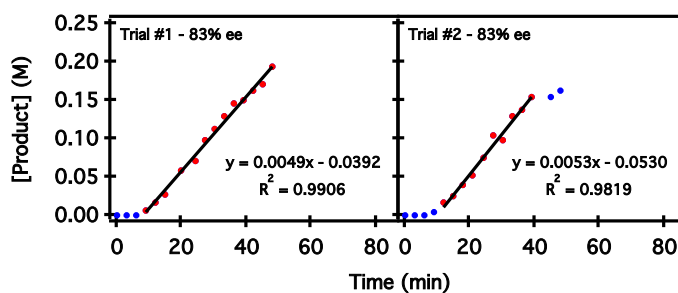


Figure 4.45 Reaction conditions with 4.0 equivalents of benzyl chloride **167**.



Effect of Other Reagent Equivalents

The general reaction procedure was followed, except the sodium iodide and zinc dust equivalents were varied. Furthermore, the general reaction ee was conducted in the presence of 4-methoxystyrene.

Figure 4.46 Reaction conditions with 6 equivalents of zinc.

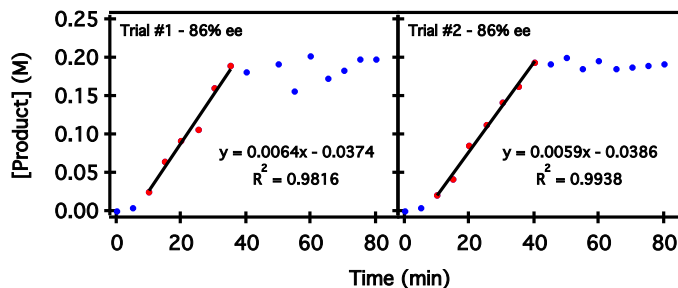


Figure 4.47 Reaction conditions without NaI.

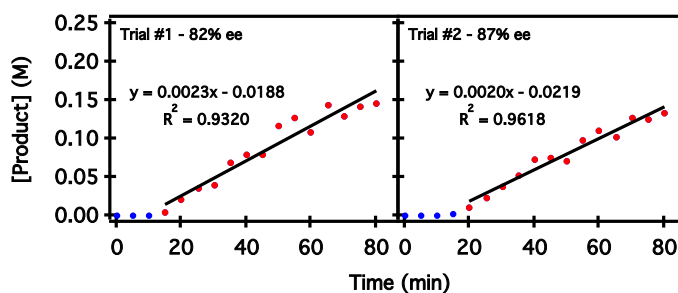
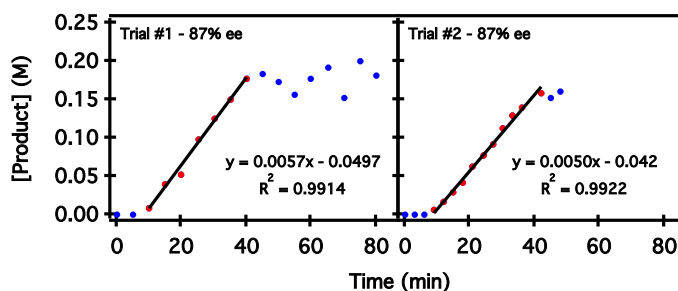


Figure 4.48 Reaction conditions with with an added equivalent of 4-methoxystyrene.



GC-FID Standards

Three standards were made to normalize the GC-FID area counts and convert the obtained data into reaction concentration (M) values. The purified reaction product and dodecane standard were each added to a 20 mL vial and massed on a balance. The mixture was

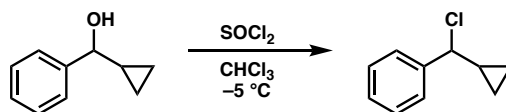
dissolved in 2 mL of ether and transferred to a GC vial for analysis. The density of dodecane (0.75 g/mL) was also used to convert the area values to concentration.

Table S5: GC-FID standards and response factors.

Trial	Mass PDT (mg)	Mass STD (mg)	PDT MW (g/mol)	STD MW (g/mol)	PDT Area	STD Area	Response Factor
A	3.6	4.6	238.33	170.33	17586	50259	0.626
B	7.0	7.1	238.33	170.33	42861	81360	0.748
C	3.7	5.5	238.33	170.33	20735	66615	0.647
						AVG	0.674

4.7.10 Radical Clock Experiments

(chloro(cyclopropyl)methyl)benzene (**198**)



The benzyl alcohol **198** (237 mg, 1.6 mmol, 1 equiv) was dissolved in 5.3 mL of CHCl_3 (purified by filtering through a plug of dried basic alumina) in a flame-dried flask under N_2 . The reaction was cooled to $-5\text{ }^\circ\text{C}$ and SOCl_2 (139 μL , 1.92 mmol, 1.2 equiv) was added. Reaction was allowed to stir for 10 minutes before being concentrated. A separate reaction sample was analyzed by ^1H and ^{13}C NMR in CDCl_3 . For the cross-coupling experiments, the concentrated sample was dissolved in anhydrous DMA to prepare **198** as a 0.2 M solution and added to the reaction without further purification. ^1H NMR (300 MHz, CDCl_3): δ 7.52 – 7.45 (m, 2H), 7.44 – 7.29 (m, 3H), 4.33 (d, $J = 9.2$ Hz, 1H), 1.70 – 1.50 (m, 1H), 0.85 (dddd, $J = 8.8, 7.9, 5.9, 4.4$ Hz, 1H), 0.78 – 0.66 (m, 1H), 0.66 – 0.56 (m,

1H), 0.46 (ddt, $J = 9.1, 5.6, 4.6$ Hz, 1H). ^{13}C NMR (75 MHz, CDCl_3): δ 141.7, 128.6, 128.3, 127.2, 69.1, 20.0, 6.6, 6.4.

(*R,E*)-1-(3-cyclopropyl-3-phenylprop-1-en-1-yl)-4-methoxybenzene (161a)

1-methoxy-4-((1*E*,5*E*)-6-phenylhexa-1,5-dien-1-yl)benzene (161b)

1-methoxy-4-((*S*,1*E*,4*E*)-3-methyl-5-phenylpenta-1,4-dien-1-yl)benzene (161c)

1-methoxy-4-((*S*,1*E*,4*E*)-3-phenylhexa-1,4-dien-1-yl)benzene (161d)



The reaction was conducted as described in literature (0.2 mmol scale) with the exception of Zn as the reductant and the benzyl chloride **198** being added as a solution in DMA.⁸ The alkenyl bromide **86** (42.6 mg, 0.2 mmol, 1 equiv), **L2**·NiCl₂ (4.8–19.4 mg, 0.01–0.04 mmol, 0.05–0.20 equiv), Zn (39.2 mg, 0.6 mmol, 3 equiv), and NaI (15.0 mg, 0.1 mmol, 0.5 equiv) were added to a round bottom flask, sealed with a septa, and purged with N₂. The flask was cooled to 0 °C before the benzyl chloride (0.2 mmol) in DMA (0.2 mL) was added. The reactions were stirred for 2 hours, then quenched with aq. 1 M HCl (10 mL), extracted with Et₂O (3 x 10 mL), and purified by column chromatography to isolate 17.3 mg (5 mol % Ni), 17.6 mg (10 mol % Ni), and 17.4 mg (20 mol % Ni) of the product mixture (**161a–d**).

4.8 REFERENCES

- (1) Weix, D. J. *Acc. Chem. Res.* **2015**, *48*, 1767.
- (2) Durandetti, M.; Gosmini, C.; Périchon, J. *Tetrahedron* **2007**, *63*, 1146.
- (3) Everson, D. A.; Shrestha, R.; Weix, D. J. *J. Am. Chem. Soc.* **2010**, *132*, 920.
- (4) Everson, D. A.; Jones, B. A.; Weix, D. J. *J. Am. Chem. Soc.* **2012**, *134*, 6146.
- (5) Wotal, A. C.; Weix, D. J. *Org. Lett.* **2012**, *14*, 1476.
- (6) Yu, X.; Yang, T.; Wang, S.; Xu, H.; Gong, H. *Org. Lett.* **2011**, *13*, 2138.
- (7) Cherney, A. H.; Kadunce, N. T.; Reisman, S. E. *J. Am. Chem. Soc.* **2013**, *135*, 7442.
- (8) Cherney, A. H.; Reisman, S. E. *J. Am. Chem. Soc.* **2014**, *136*, 14365.
- (9) Hofstra, J. L.; Cherney, A. H.; Ordner, C. M.; Reisman, S. E. *J. Am. Chem. Soc.* **2018**, *140*, 139.
- (10) Suzuki, N.; Hofstra, J. L.; Poremba, K. E.; Reisman, S. E. *Org. Lett.* **2017**, *19*, 2150.
- (11) Kadunce, N. T.; Reisman, S. E. *J. Am. Chem. Soc.* **2015**, *137*, 10480.
- (12) Poremba, K. E.; Kadunce, N. T.; Suzuki, N.; Cherney, A. H.; Reisman, S. E. *J. Am. Chem. Soc.* **2017**, *139*, 5684.
- (13) Biswas, S.; Weix, D. J. *J. Am. Chem. Soc.* **2013**, *135*, 16192.
- (14) Ren, Q.; Jiang, F.; Gong, H. *J. Organomet. Chem.* **2014**, *770*, 130.
- (15) Anka-Lufford, L. L.; Huihui, K. M. M.; Gower, N. J.; Ackerman, L. K. G.; Weix, D. J. *Chem. Eur. J.* **2016**, *22*, 11564.
- (16) Suh, Y.; Lee, J.; Kim, S.-H.; Rieke, R. D. *J. Organomet. Chem.* **2003**, *684*, 20.
- (17) Peng, Z.; Knochel, P. *Org. Lett.* **2011**, *13*, 3198.

- (18) Benischke, A. D.; Breuillac, A. J. A.; Moyeux, A.; Cahiez, G.; Knochel, P. *Synlett* **2016**, 27, 471.
- (19) Benischke, A. D.; Desaintjean, A.; Juli, T.; Cahiez, G.; Knochel, P. *Synthesis* **2017**, 49, 5396.
- (20) Breitenfeld, J.; Wodrich, M. D.; Hu, X. *Organometallics* **2014**, 33, 5708.
- (21) Chen, C.-T.; Liao, S.-Y.; Lin, K.-J.; Chen, C.-H.; Lin, T.-Y. *J. Inorg. Chem.* **1999**, 38, 2734.
- (22) Vanýsek, P. *Handbook of Chemistry and Physics*, 93rd ed.; 2012.
- (23) Jones, G. D.; Martin, J. L.; McFarland, C.; Allen, O. R.; Hall, R. E.; Haley, A. D.; Brandon, R. J.; Konovalova, T.; Desrochers, P. J.; Pulay, P.; Vicic, D. A. *J. Am. Chem. Soc.* **2006**, 128, 13175.
- (24) Schley, N. D.; Fu, G. C. *J. Am. Chem. Soc.* **2014**, 136, 16588.
- (25) Oderinde, M. S.; Frenette, M.; Robbins, D. W.; Aquila, B.; Johannes, J. W. *J. Am. Chem. Soc.* **2016**, 138, 1760.
- (26) Zhao, P.; Luo, Y.-W.; Xue, T.; Zhang, A.-J.; Lu, J.-X. *Chinese J. Chem.* **2006**, 24, 877.
- (27) Ge, P.; Riordan, C. G.; Yap, G. P. A.; Rheingold, A. L. *Inorg. Chem.* **1996**, 35, 5408.
- (28) Halgren, T. A.; Roberts, J. D.; Horner, J. H.; Martinez, F. N.; Tronche, C.; Newcomb, M. *J. Am. Chem. Soc.* **2000**, 122, 2988.
- (29) *Encyclopedia of Radicals in Chemistry, Biology and Materials*; John Wiley & Sons, Ltd., 2012.
- (30) Buskirk, A.; Baradaran, H. *J. Chem. Educ.* **2009**, 86, 551.

- (31) Still, W. C.; Kahn, M.; Mitra, A. *J. Org. Chem.* **1978**, *43*, 2923.
- (32) Evans, D. A.; Downey, C. W.; Hubbs, J. L. *J. Am. Chem. Soc.* **2003**, *125*, 8706.